The Pennsylvania State University

The Graduate School

LIGHT-POWERED FLUID MICROPUMPS FOR ASSEMBLY AND SENSING

A Dissertation in

Chemistry

by

Benjamin Tansi

Submitted in Partial Fulfillment
of the Requirements
for the Degree of

Doctor of Philosophy

August 2020

The dissertation of Benjamin Tansi was reviewed and approved by the following:

Ayusman Sen
Verne M. Willaman Professor of Chemistry
Professor of Chemistry
Professor of Chemical Engineering
Dissertation Advisor
Chair of Committee

Thomas E. Mallouk
Evan Pugh Professor
DuPont Professor of Materials Chemistry and Physics
Professor of Biochemistry and Molecular Biology

Christine D. Keating
Distinguished Professor of Chemistry

Darrel Velegol
Distinguished Professor of Chemical Engineering

Phil C. Bevilacqua
Distinguished Professor of Chemistry
Distinguished Professor of Biochemistry and Molecular Biology
Head of the Department of Chemistry

ABSTRACT

The field of active matter has received considerable attention since it began in 2004. Although the bulk of this research has focused on potential drug-delivery systems, this technology may reach a much wider range of applications. Under the conditions that motion is controlled and directed, any colloid could offer new and deeper functionalities. For example, consider a paint that self-deposits or aggregates controllably. Perhaps imagine a plasmonic nanoparticle that will seek out its neighbors as a step to assemble solar cells. Alternatively, carefully controlled motion can serve in sensing applications so long as we know the conditions upon which its rate or direction depends. If a micropump predictably responds to the concentration of certain analytes, you will be able to determine the nature or concentration of the species present. Given this simple principle, it pays to build a catalog of analytes and methods. That is, if you want to test the concentration of different compounds, you will need to develop different pumps. The objective of this present undertaking is to first prove that plasmonic nanoparticles can generate convective fluid pumping to perform tasks such as colloidal crystal assembly. This is followed by methods to separate particles investigation of particle size and. After considering ways to affect the pumping rates, we introduce a strategy to control direction using specific photo-reactions.

TABLE OF CONTENTS

LIST OF FIGURES

LIST OF TABLES

LIST OF MULTIMEDIA FILES

The videos described herein are used with permission from the references at the start of their respective chapters.

Supporting Video **2-1**: Tracer particles (10 μm polystyrene) in a suspension of TiO2 (360±70 nm, 0.007% w/v) before and after UV irradiation (speed 4x). This was taken at 1140 μm above the bottom surface and observed using a 5x objective.

Supporting Video **2-2**: Outwards flow closer to the top of the solution (speed 4x). Tracer particles (10 μm polystyrene) in a suspension of TiO2 (360±70 nm, 0.007% w/v) before and after UV irradiation. This was taken at 2400 μm above the bottom surface and observed using a 5x objective.

Supporting Video **2-3**: Observation of convective rolls in a glass-sided chamber (speed 16x). The TiO2 particles (2 mg/mL, 360±70 nm) were allowed to settle to the bottom of the chamber overnight before being irradiated from below with ultraviolet light. The chamber had a height of 1.2 cm and a width of 0.4 cm. It was cut to be 7 cm long. Further details are given in Section **2.3.5**.

Supporting Video **2-4**: The collection of 10 μm polystyrene particles during UV irradiation in a TiO2 (0.007% w/v, 360±70 nm) suspension (speed 300x). This was observed using a 20x objective. The flows near the surface will carry the particles towards the region being irradiated and press them into a close-packed colloidal crystal monolayer. A small amount of sodium nitrate (0.14 mM) was added to mitigate buckling.

Supporting Video **2-5**: Fluid pumping by a TiO2 patch (speed 6x). The lamp is on at all times, but flows do not develop until the light is directed towards the patch at which case they begin spontaneously. This was taken at 1140 μm above the bottom surface and observed using a 5x objective. This pumping can be seen by 10 μm polystyrene tracer particles.

Supporting Video **2-6**: The migration of a particle ensemble due to bulk flows from gold (0.0007% w/v, 21±5 nm) (Speed 300x). After collecting, the light and the frame are moved to the right at which point the assembled colloidal crystal structure breaks and migrates to the new location. During this transition, grain boundaries can be seen to constantly form and anneal.

Supporting Video **2-7**: The simulations of the aggregation of the polystyrene tracers by the convective flow. Initially, tracers (blue spheres) are uniformly dispersed throughout the solution. The values of temperature $T-T_0$ are shown by the color-bar. The part of the fluid domain exposed to light is indicated by the red circles in the "Top

view" and by the higher temperatures in the "Side view". The directions of the generated convective flow are shown with black arrows. The concentration of gold nanoparticles (not shown) is C=0.005% w/w and each particle produces heat q = 1.39 pW.

Supporting Video **2-8**: Simulations of the migration of tracer particles due to the relocation of the light (red circle). Initially, tracers (blue spheres) are uniformly dispersed throughout the solution. The values of temperature T −T0 are shown by the color-bar. The part of the fluid domain exposed to light is indicated by the red circles in the "Top view" and by the higher temperatures in the "Side view". The directions of the generated convective flow are shown with black arrows. The concentration of gold nanoparticles (not shown) is C=0.005 % w/w and each particle produces heat q = 1.39 pW.

Supporting Video **3-1**: A video of 3, 10, and 20 μm particles moving along a surface due to light-powered, convective pumping. Since larger particles feel the higher flow rates away from the surface, they migrate faster towards to center where the light is fixed. 5 nm AgNPs (0.0011% w/w) were used in this trial and the bottom of the frame is 1528.8 μm across. 64x speed.

Supporting Video **4-1**: The fluid pumping reversal for a solution of ethanol (0.217 M) and hydrogen peroxide (0.49 M) under UV irradiation. Shortly after the light is turned on, the pumping direction will change from upwards to downwards. 16x speed.

Supporting Video **4-2**: The near-surface fluid motion stemming from diffusioosmosis. Despite the outward motion of the bulk solution, particles will move inward upon reaching the surface. This trial was created using glycerol (0.217 M) and hydrogen peroxide (0.49 M) under UV irradiation. 256x speed.

Supporting Video **4-3**: The surface migration of 10μm and 20μm tracer particles during the upward pumping of acetaldehyde/H2O2 solution with added CTAB under irradiation. Due to the inward motion of the bulk solution, larger particles will move inward since they extend further into the solution. Smaller particles will instead respond to the near-surface diffusioosmotic pumping and will instead move outward. 128x speed.

Supporting Video **5-1**: The change in pumping direction of a solution of photoacid generator. A solution of 0.29mM N-hydroxynaphthalamide triflate and 100mM sodium nitrate was prepared in water with N-methyl pyrrolidone as a co-solvent (14%). When the light is turned on, the solution will begin to pump inward. When the light is turned off, the direction immediately changes to downwards. 16x speed.

ACKNOWLEDGEMENTS

It is only appropriate that I begin by acknowledging my advisor, Ayusman Sen. His guidance (and patience) has helped me tremendously throughout these years and it is hard to imagine graduate school without his tutelage. He is also largely responsible for the cast of characters around me during this time. I have had the great fortune of working with good-humored and incredibly talented colleagues. I can't overstate how much I appreciate your company and input as well as the endless memories from years of general shenanigans, endless cake, and the moments that warranted it.

There are many people who need to be acknowledged for leading me down the path of science to begin with. This is most true for my parents, Joan and Bill Tansi. Because of the sense of curiosity that you fostered in me, it wasn't so much a question of whether I would pursue science, but what field I would go into. This question was eventually resolved by Peter Gaudet who introduced me to the seemingly endless world of chemistry. This was cemented by the passion and knowledge of my professors at Juniata College. I would especially like to thank Don Mitchell for helping me come to appreciate polymer chemistry, for taking me on as a research student, and for our occasional lunch outings since then.

Let me also extend my appreciation to the Otter Pockets, the unofficial intramural soccer team of the chemistry department, as well as to the Vikings in the Nittany Hockey League. You have made State College feel like my home. Thank you to Scott Gorman, who was an incredible roommate for 4 years, and to Chris Rumble who made us both appreciate the beauty of central Pennsylvania through many hikes and mountain bike outings. And of course, a deep-felt thank you to Marissa Saladin for keeping my head on straight for five years.

Chapter 1

Introduction: Powered Motion at Small Scales

In 2004, a group of scientists at the Pennsylvania State University made an astonishing discovery. A bimetallic nanorod in a bath of hydrogen peroxide could be seen to propel itself through solution.[1] By directing an asymmetric breakdown of a reactant, these rods would spontaneously generate an electric field and respond to it by moving.[2] Although the principle wasn't nailed down initially, this "nanomotor" was able to capture the imaginations of many. In his 1966 book, "Fantastic Voyage," author Isaac Asimov had explored a future within which maladies were treated via nano-surgery. Upon seeing a self-propelled nanoscale object, this suddenly seemed attainable and the field of active matter grew rapidly. Modifications were quickly made to allow for magnetic steering by adding nickel stripes to the rod.[2] Even without this addition, these motors were seen to move directionally towards a source of their fuel,[3] a so-called "chemotaxis," usually associated with microscopic organisms. This provided an appealing strategy by which to target tumors, which excrete high concentrations of hydrogen peroxide.[4]

In short order, they realized that the principles governing self-propulsion could be applied much more broadly. According the Gallilean invariance, a motor fixed in place would instead propel the fluid around it.[5,6] These "micropumps" quickly gained their own place in the motors community, but offered a much different suite of potential applications. These combined innovations launched the beginning of an incredible saga, but there were many challenges uncovered along the way. This chapter will discuss these challenges and then explore some of the methods by which scientists have navigated around them.

1.1 Challenges and Considerations

Provided an energy input, asymmetry yields directionality. This simple principle belies the many hurdles facing scientists in the field of active matter. In order to develop a viable therapeutic agent or diagnostic test, we need to first appreciate the unusual conditions experienced at small scales.

1.1.1 Brownian Motion

In order to undergo self-propulsion, a motor needs to overcome two important limitations. The first of these is Brownian motion. This behavior was first documented in 1827 by its namesake, John Brown, who noted that pollen granules would undergo "rapid oscillatory motion" when observed in water under a microscope. This behavior was so astounding that he proceeded to test any pollen at his disposal before trying again with pollen from dead plants and finally fine powder from rocks.[7] Suffice it to say that they all exhibited similar behavior.

A picture of this motion wasn't clearly developed until the early 20th century. Building on the pioneering work of George Stokes, an up-and-coming physicist named Albert Einstein was able to describe diffusive behavior fully in what we now know as the Stokes-Einstein Equation.

$$D_t = \frac{kT}{6\pi\eta a} \tag{1.1}$$

Here, k is the Boltzmann constant, T the temperature, η is the viscosity, and a represents the radius. In the design of nanomotors, the relation between the radius and diffusion is of particular note. The smaller the particle, the faster that it diffuses. The rotational diffusion only complicates the matter further.

$$D_r = \frac{kT}{8\pi\eta a^3} \tag{1.2}$$

As given, the rotational diffusion relates to the cube of the radius. Together, these equations set the requirements for attaining any level of directionality. The smaller the motor, the greater the hurdles.

1.1.2 Reynolds Number

When considering problems in fluid mechanics, it is useful to first consider the Reynolds number (*Re*). Simply, the Reynolds number is the dimensionless ratio of the inertial and viscous forces, given as

$$Re = \frac{\rho U a}{\eta} \tag{1.3}$$

Where ρ is the density, U is the velocity, a is the characteristic length-scale (radius in our case), and η is the viscosity. For useful context, the Reynolds number of a person swimming in water is around 10^4. One of the implications of this is that we continue to move when we dive into a pool due to the dominating inertial effects. Bacteria, on the other hand, have a Reynold's number of about 10^{-4}. Given such a low Reynolds number, if any propelling force should cease, the bacteria will halt immediately. Whatever inertia is held by a single bacterium is meaningless given the, now insurmountable, viscous forces of water. Motion can only be achieved by the steady application of force in order to break symmetry and ensure nonreciprocal motion.

1.1.3 Electric Double Layer

While not so much a challenge, an understanding of the electric double layer is vital in order to address the design of both nanomotors as well as fluid micropumps such as that discussed in chapter 4. As such, it warrants a brief introduction. An illustration of a particle in solution is provided in Figure 1.1.

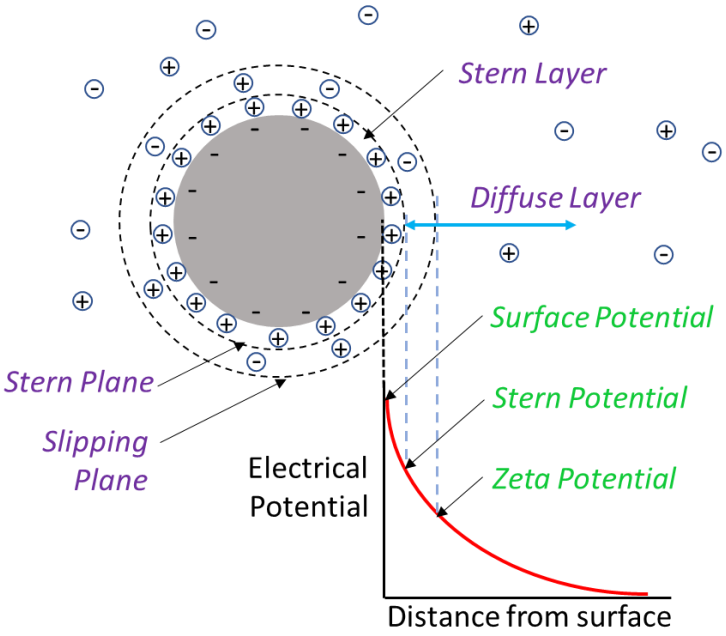

Figure **1-1**: An illustration of the double layer structure around a negatively charged particle in solution.

When a charged surface is introduced into solution, a cloud of oppositely charged ions will collect around it in order to neutralize the charge. Near to the surface is a loosely adsorbed layer of oppositely charged ions in what is called the "Stern layer." Outside of this is a diffuse layer of ions which contains what is termed the slipping plane. Perhaps best described as "notional," the slipping plane is a layer within which the solution is understood to move with the particle.[8] It is at this plane that the zeta potential is measured. Intuitively, one would expect the surface charge

to be the primary concern in predicting behavior, however, the zeta potential is generally the value considered since it reflects the environment of the particle as well as its charge. As one may expect, high salt concentrations will quench the surface charge. This has vital implications for controlling aggregation, and some phoretic transport mechanisms. It can also be a powerful tool in determining the underlying mechanism of novel active matter results.

1.2 Strategies to Drive Microscale Motion

Having acknowledged these hurdles, this section will now explore the ways to overcome them. First will be a brief discussion on the mechanisms found in nature and the ways that scientists have channeled it. This will be followed by some of the principles that have been used to generate motion in synthetic systems. Only those methods that are relevant to the present dissertation will be discussed. Note that there is an expansive list of different nanomotors and pumps as well as some excellent reviews on this topic.[9–11]

1.2.1 Nature's Techniques

To overcome the above limitations, bacteria have evolved to have all sorts of strategies for motility. The most prominent of these is perhaps flagella, which serve as a propeller to yield steady propulsion. Some research groups have exploited their incredible efficiency by tethering a cargo to the cell and using the whole unit as a motor.[12–14] A lesser known, but fascinating method is that of listeria monocytogenes, which propels itself by the rapid polymerization of intracellular actin filaments, effectively "squeezing" the organism forward while a tail grows behind it.[15] This has also been used in synthetic systems.[16] By binding the protein responsible for polymerization to

the outside of a microparticle, the particle would propel in an actin rich environment. On the other team are white blood cells, which display characteristic tendrils as they move through solution via their own actin polymerization/de-polymerization mechanism.[17]

Looking to even smaller scales, there are a host of transport methods within the cells themselves. The most notable of these is the treadmilling action of myosin and kinesis on actin microtubules.[18] On a myosin functionalized surface, actin tubules will move so long as adequate ATP is present in the system.[19] Single enzymes themselves have demonstrated their own motility in what has been termed "enhanced diffusion" as well as some degree of chemotaxis.[20–22] Given their diameters, directed motion would seem impossible when considering how diffusion with size. However, increased, non-directed motion is viable. The mechanism of action has been a contested point for many enzymes; however, it has been seen that enzyme turnover will fluidize the cellular environment.[23] Further, enzymes have been used to drive the motion of nanoparticles when bound to their surface.[24–27] Given a high local concentration, these enzymes can be used as fluid micropumps, which will be discussed further in the next section.

1.2.2 Thermophoresis and Density-Driven Convection

Thermal methods of propulsion can be broadly sorted into two categories, which cleanly divide motors and micropumps. Nanomotors powered by heat are generally driven by thermophoresis, sometimes referred to as the Soret effect. With few exceptions, particles in solution will move from hotter regions to colder ones.[28,29] Although the motion stems from heating, the energy input may vary, typically between using light irradiation[28,30,31] or magnetic fields.[32]

The other category is motion driven by convection. A fabricated region that yields heat will introduce the asymmetry needed to induce motion. Because of how ubiquitous this feature is, even micropumps that are *not* based on thermal convection should account for its presence or lack thereof. Some examples of enzyme micropumps are also powered by thermal convection.[33] An illustration of one of these pumps is given in Figure **1-2**. Here, a small, enzyme-functionalized gold patch is centered in a fluid filled hybridization chamber. In a solution of the enzyme's respective substrate (reactant), catalysis will occur about the patch and heat will begin to develop in the immediate area due to its exothermic nature. As the temperature increases, the density decreases and fluid is swept up and away from the patch. These micropumps have now been used to detect toxins[34] and have also been integrated into hydrogels to controllably leach insulin.[33]

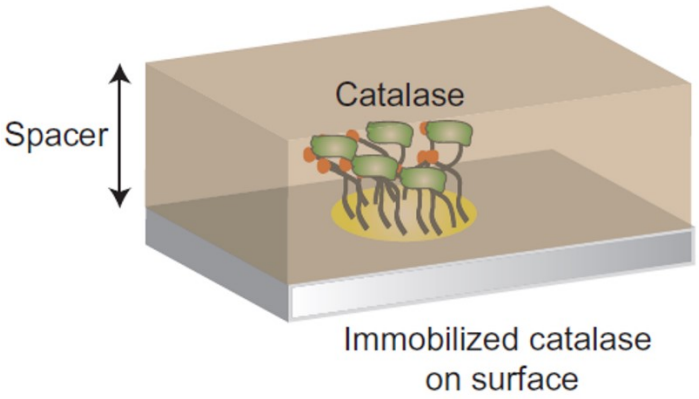

Figure **1-2**: From Ref. 33. An illustration of a micropump based on the catalytic turnover of catalase. When a solution of substrate is introduced, enzymes tethered to a gold patch will undergo an exothermic reaction, thereby yielding heat locally.

Micropumps based on thermal convection are part of yet a broader group of density-driven convective pumps. As temperature increases, the density of solution will decrease, mirroring other mechanisms. Density-based micropumps have also been made using host-guest interactions,[35] trans-esterification,[36] and the photothermal effect.[36,37] Additionally, there are some examples in

which product formation will actually increase the solutal density and drive pumping downwards.[38,39]

1.2.3 Electrophoresis and Electroosmosis

The principle of electrophoresis should be familiar to any biochemist. Most often, this comes up in the form of gel plates as a means to qualify proteins and DNA fragments using an electric field. On account of its ubiquitous use, it should come as little surprise that it has been applied in the design of nanomotors. If you recall the bimetallic rod from the introduction to this chapter, electrophoresis was at play from the beginning.

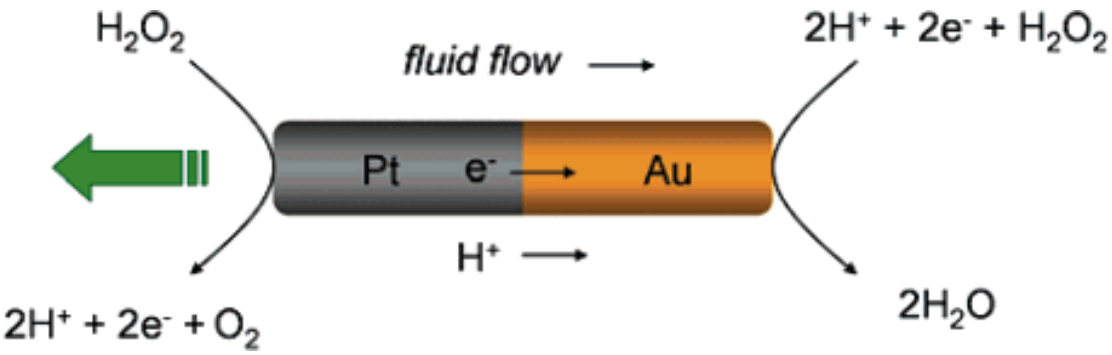

Figure **1-3**: From Ref. 40. The mechanism of action of the bimetallic nanorod. Due to separate redox reaction on either end of the rod, a build-up of protons will occur on the platinum end. The rod will respond to the electric field that develops according to electrophoresis.[40]

In brief, electrophoresis is the motion ("phoresis" or migration) of particles within an electric field. Simply, a particle will respond to an electric field and it will move due to its own surface charges according to the "opposites attract" principle. Given this, the "self" part should be evident. Simply, a particle that generates a gradient will in effect respond to itself based on its own surface charge. In the case of these motors, hydrogen peroxide was broken down asymmetrically

by the platinum and gold halves of the nanorod shown in Figure 1-1. In doing so, a build-up of protons developed on one end of the rod and the negatively charged nanorod propelled towards them.

As a general rule, electrophoresis will occur with a related mechanism called electroosmosis.[41] As "osmosis" generally refers to the motion of water, 'electroosmosis" refers to the motion of water due to an electric field along a charged surface. As described by the double layer model (section 1.1.3), a region of oppositely charged ions will develop around a charged surface in order to neutralize it. Given this bias, the layer will respond to an applied electric field in the form of motion, again according to the "opposites attract" principle. As the ions move, so too will the water that was solvating it. This effect will also contribute to the motor above as the flow of protons will carry water with them. In this manner, the motors will move in much the same way as a team of rowers propel themselves by directing the water around them.

Electrophoretic velocity can generally be described by the Smoluchowski equation for thin double layers.[41,42]

$$U_{ep} = \frac{\zeta_p \varepsilon}{\mu} E \tag{1.4}$$

Here, ζ_p is the zeta potential of the particle, ε is the permittivity of solution, E is the electric field strength, and μ is the dynamic viscosity. Electroosmosis uses the same equation except for a change in sign on the zeta potential, which now describes the wall.

$$U_{eo} = \frac{-\zeta_w \varepsilon}{\mu} E \tag{1.5}$$

The change in sign is because the velocity is not of the wall, but of solution, for which the charge sign is *opposite*. In the case of our nanorod, this means that proton rich fluid is driven away from the proton source (the platinum end. Figure **1-3**) and therefore pushes the rod in the same

direction as it moves under electrophoresis. In this case, the two effects compound. However, this is not always the case as either mechanism can dominate depending on the conditions.[40] The net velocity is additive as such,

$$U_{tot} = U_{ep} + U_{eo} \tag{1.6}$$

The principle of electroosmosis can be seen more clearly in the case of micropumps. Upon developing the bimetallic nanorod, these same researchers experimented with binding the metals to a surface.[5] Seeing as the "motor" could no longer move, the solution around it began towards the patch. To preserve fluid continuity, convective flows develop.

1.2.4 Diffusiophoresis and Diffusioosmosis

To be concise, diffusiophoresis is electrophoresis with extra steps. As the prefix (diffusio-) suggests, it is motion (-phoresis) stemming from diffusion. Like microparticles, ions will also diffuse in solution (Section 1.1), and like particles, smaller ions diffuse faster, which has fascinating implications. J.L. Anderson was able to explore this mechanism using a permeable membrane separating a salt solution from deionized water.[43] Upon introduction, the ions from the salt solution would diffuse into the side with pure water. However, since the smaller ions diffused faster, and since ions are charged, a local electric field would develop and *electro*phoresis would then push around any tracer particles that were caught in it.

Diffusioosmosis is motion *of water* stemming from diffusion. One of the best examples of this was done by an engineer named Joe McDermott in 2012.[44,45] His experiment was very simple, he wanted to see what would happen to the surrounding medium while a salt crystal was dissolving. A crystal of calcium carbonate was added to solution and some negatively charged tracer particles

were used to observe the motion of the fluid. They were seen to rush away from the crystal. The dissolution products of calcium carbonate are Ca^{2+}, OH^-, and HCO_3^-, of which Ca^{2+} has the lowest diffusivity. With the anions diffusing faster, the electric field points outward. Thus, near-surface cations and their solvating water molecules move out with it, carrying the tracer particles in the flow. This principle has also been used to design micropumps based on photo-acid generators and a polymeric imine.[46]

It should be noted that the above only describes "electrolyte self-diffusiophoresis." Non-electrolyte diffusiophoresis has also been explored. A more comprehensive investigation is given in Ref. 42.

1.3 Conclusions

The principles discussed above relate directly to the findings in the following chapters. In Chapter 2, the photothermal effect is exploited using plasmonic nanoparticles to generate local heating and then motion. This is used to assemble colloidal crystals, which can move controllably. Chapter 3 builds on this finding through several investigations. These include a particle separation method based on size and an exploration of particle types for pumping derived from ultraviolet light. Chapter 4 introduces a method to cause downwards pumping via organic photochemistry. Using this approach, we are able to produce two flow regimes that can be tuned independently of each other. After reviewing these works, Chapter 5 focuses on what investigations should follow.

1.4 References

[1] W. F. Paxton, K. C. Kistler, C. C. Olmeda, A. Sen, S. K. St. Angelo, Y. Cao, T. E. Mallouk, P. E. Lammert, V. H. Crespi, *J. Am. Chem. Soc.* **2004**, *126*, 13424–13431.

[2] T. R. Kline, W. F. Paxton, T. E. Mallouk, A. Sen, *Angew. Chem. Int. Ed.* **2005**, *44*, 744–746.

[3] Y. Hong, N. M. K. Blackman, N. D. Kopp, A. Sen, D. Velegol, *Phys. Rev. Lett.* **2007**, *178103*, 1–4.

[4] T. P. Szatrowski, C. F. Nathan, *Cancer Res.* **1991**, *51*, 794–799.

[5] T. R. Kline, W. F. Paxton, Y. Wang, D. Velegol, T. E. Mallouk, A. Sen, *J. Am. Chem. Soc.* **2005**, *127*, 17150–17151.

[6] M. E. Ibele, Y. Wang, T. R. Kline, T. E. Mallouk, A. Sen, *J. Am. Chem. Soc.* **2007**, *129*, 7762–7763.

[7] R. Brown, *Philos. Mag.* **1828**, *4*, 161–173.

[8] J. Jiang, G. Oberdörster, P. Biswas, *J. Nanopart. Res.* **2009**, *11*, 77–89.

[9] F. Wong, K. K. Dey, A. Sen, *Annu. Rev, Mater. Res.* **2016**, *46*, *407-432*.

[10] K. K. Dey, A. Sen, *J. Am. Chem. Soc.* **2017**, *139*, 7666-7676.

[11] S. Sánchez, L. Soler, J. Katuri, *Angew. Chem. Int. Ed.* **2015**, *54*, 1414–1444.

[12] M. Kojima, Z. Zhang, M. Nakajima, T. Fukuda, *Biomed Microdevices* **2012**, *14*, 1027–1032.

[13] V. Magdanz, S. Sanchez, O. G. Schmidt, *Adv. Mater.* **2013**, *25*, 6581–6588.

[14] V. Magdanz, O. G. Schmidt, *Expert Opin. Drug Deliv.* **2014**, *11*, 1125-1129.

[15] N. CHAFFEY, *Ann. Bot.* **2003**, *91*, 401.

[16] L. A. Cameron, M. J. Footer, A. Van Oudenaarden, J.A. Theriot, *Proc. Natl. Acad. Sci* **1999**, *96*, 4908–4913.

[17] T. D. Pollard, G. G. Borisy, *Cell* **2003**, *112*, 453–465.

[18] S. M. Block, *Cell*, **1998**, *93*, 5–8.

[19] S. J. Kron, J. A. Spudich, *Proc. Natl. Acad. Sci.* **1986**, *83*, 6272–6276.

[20] S. Sengupta, K. K. Dey, H. S. Muddana, T. Tabouillot, M. E. Ibele, P. J. Butler, A. Sen, *J. Am. Chem. Soc.* **2013**, *135*, 1406–1414.

[21] H. S. Muddana, S. Sengupta, T. E. Mallouk, A. Sen, P. J. Butler, *J. Am. Chem. Soc.* **2010**, *132*, 2110–2111.

[22] K. K. Dey, S. Das, M. F. Poyton, S. Sengupta, P. J. Butler, P. S. Cremer, A. Sen, *ACS Nano* **2014**, *8*, 11941–11949.

[23] B. R. Parry, I. V. Surovtsev, M. T. Cabeen, C.S. O'Hern, E. R. Dufresne, C. Jacobs-Wagner, *Cell* **2014**, *156*, 183–194.

[24] I. -L. Pavel, A. -I. Bunea, S. David, S. Gáspár, *Chem. Cat. Comm.* **2014**, *6*, 866–872.

[25] A. -I. Bunea, I. -A. Pavel, S. David, S. Gáspár, *Chem. Comm.* **2013**, 8803–8805.

[26] K. K. Dey, X. Zhao, B. M. Tansi, R. Golestanian, A. Sen, *Nano. Lett.* **2015**, *15*, 8311-8315

[27] X. Ma, A. Jannasch, U. -R. Albrecht, K. Hahn, A. Miguel-López, E. Schäffer, S. Sánchez, *Nano. Lett.* **2015**, *15*, 7043-7050.

[28] H. R. Jiang, N. Yoshinaga, M. Sano, *Phys. Rev. Lett.* **2010**, *105*, 1–4.

[29] S. Iacopini, R. Rusconi, R. Piazza, *Eur. Phys. J. E* **2006**, *19*, 59–67.

[30] K. Villa, M. Pumera, *Chem. Soc. Rev.* **2019**, *48*, 4966–4978.

[31] C. Maggi, F. Saglimbeni, M. Dipalo, F. De Angelis, R. Di Leonardo, *Nat. Commun.*, **2015**, *6* 7855-7859.

[32] L. Baraban, R. Streubel, D. Makarov, L. Han, D. Karnaushenko, O. G. Schmidt, G. Cuniberti, *ACS Nano.* **2013**, *7*, 1360–1367.

[33] S. Sengupta, D. Patra, I. Ortiz-Rivera, A. Agrawal, S. Shklyaev, K. K. Dey, U. Córdova-Figueroa, T. E. Mallouk, A. Sen, *Nat. Chem.* **2014**, *6*, 415–422.

[34] I. Ortiz-Rivera, T. M. Courtney, A. Sen, *Adv. Funct. Mater.* **2016**, *26*, 2135–2142.

[35] D. Patra, H. Zhang, S. Sengupta, A. Sen, *ACS Nano*, **2013**, *7*, 7674–7679.

[36] Y. Guo, D. Wang, J. Li, Y. Sun, M. Li, H. Zhang, R. Duan, D. Zhang, B. Song, B. Dong, *J. Mater. Chem. C.* **2019**, *7*, 2299–2304.

[37] J. S. Donner, G. Baffou, D. McCloskey, R. Quidant, *ACS Nano* **2011**, *5*, 5457–5462.

[38] I. Ortiz-Rivera, H. Shum, A. Agrawal, A. Sen, A. C. Balazs, *Proc. Natl. Acad. Sci.* **2016**, *113*, 2585–2590.

[39] M. Li, Y. Su, H. Zhang, B. Dong, *Nano Res.* **2017**.

[40] W. F. Paxton, P. T. Baker, T. R. Kline, Y. Wang, T. E. Mallouk, A. Sen, *J. Am. Chem. Soc.* **2006**, *128*, 14881–14888.

[41] T. R. Kline, J. Iwata, P. E. Lammert, T. E. Mallouk, A. Sen, D. Velegol, *J. Phys. Chem. B.* **2006**, *110*, 24513–24521.

[42] C. Zhou, H. Zhang, Z. Li, W. Wang, *Lab. Chip* **2016**, *16*, 1797–1811.

[43] J. P. Ebel, J. L. Anderson, D. C. Prieve, **1988**, *7*, 396–406.

[44] D. Velegol, in *Colloid. Syst.*, **2016**, pp. 95–111.

[45] J. J. Mcdermott, A. Kar, M. Daher, S. Klara, G. Wang, A. Sen, D. Velegol, *Langmuir* **2012**, *28*, 15491-15497.

[46] V. Yadav, H. Zhang, R. Pavlick, A. Sen, *J. Am. Chem. Soc.* **2012**, *134*, 15688–15691.

Chapter 2

Solutal Pumping by the Photothermal Effect

The work in this chapter is adapted with permission from Tansi, B.T.; Peris, M.P.; Shklyaev, O.E.; Balazs, A.C.; Sen, A. Organization of Particle Islands through Light-Powered Fluid Pumping, *Angew. Chem. Int. Ed.* **2019**, *38*, 2295-2299, Copyright 2019 Wiley-VCH Verlag GmbH & Co.

This chapter outlines a method by which to generate directed fluid pumping using the photothermal effect. Using plasmonic nanoparticles to induce convection, colloidal crystals can be assembled and moved. The following sections describe the experimental results of these trials. Detailed simulations are outlined in Appendix A. The videos discussed in this chapter refer to those in the supporting information of above reference.

2.1 Introduction

The field of synthetic active matter was initiated by the findings of Paxton et al. in 2004.[1] The authors constructed a bimetallic nanorod that could autonomously propel itself through solution by asymmetrically breaking down a chemical fuel. Since then, many examples of "motors" have been reported.[2–5] When motors are affixed to a surface, they propel the surrounding fluid, in essence acting as a fluidic micropump.[6] This in turn has led to the development of a host of reaction-based pumping systems featuring different materials and mechanisms.[6–8] Such approaches eventually encompassed biology through the clever usage of enzyme molecules to yield pumping.[9] However, the use of external energy sources has the added benefit of selective initiation and termination without needing to directly contact the system. Particularly attractive is the use of

light as the external energy source owing to its ease of application and a high degree of control. Because of these advantages, the field of optofluidics has recently gained traction. Some studies have focused on the ability of metal patches to generate heat, but these require complex fabrication procedures.[10,11] Herein, a method is presented to attain comparable control over fluid pumping without the need for prefabrication or preassembly of any kind.

2.2 Results and Discussion

This section discusses a series of experiments that explore the ability to drive bulk fluid pumping according to a photothermal mechanism. This is followed by an analysis of the assembly and motility of colloidal crystals yielded in this manner. A model was developed for these experiments and is discussed at length in Appendix A.

2.2.1 Light-Powered Convection

When materials are irradiated by light, a transduction between optical and mechanical energy can occur through an opto-chemical or opto-thermal route. Notably, metallic catalysts can participate in both these mechanisms. With respect to the opto-chemical transduction, the high photocatalytic activity of titanium dioxide (TiO_2), which absorbs strongly in the ultraviolet region, enables TiO_2 microparticles to drive oxidation-reduction reactions and thereby undergo self-propulsion.[12,13] This motion can occur through diffusiophoresis, which arises in response to a nonuniform distribution of ionic products around the particles. In addition to promoting photocatalytic activity, the absorbed optical energy is transduced into heat around irradiated particles. Govorov et al. noted the existence of fluid flows when a suspension of gold nanoparticles

were irradiated using a laser at their plasmon resonance wavelength.[14] Beyond this finding, little attention has been paid to bulk fluid flows that are thermally activated by the irradiation of particles. To fill this gap, we examined the ability of TiO_2 microparticles, exposed to UV light, to generate thermally driven convective flows and harness this mechanism to assemble colloidal crystal monolayers. Such lattice structures are comprised of highly organized nano- and micron-scale particles and have gained attention due to their potential in sensors, coatings, and optoelectronics.[15,16] To provide a benchmark, we compare the behavior of the TiO_2 system to the well-studied heat generation by irradiated gold nanoparticles dispersed in an aqueous solution.[17–20]

2.2.2 Experimental Results Using Titanium Dioxide

When a beam of ultraviolet light is focused on a suspension of titanium dioxide nanoparticles, the solution immediately begins to flow convectively about the region being irradiated. This was observed in a 1 cm diameter steel-walled chamber with glass cover slips on top and bottom. The suspension was irradiated from below through a microscope objective. An illustration of this system is provided below in Figure **2-1.**

The velocity of this fluid flow was observed to increase linearly with particle density. This is highlighted in Figure **2-3A**, in which the particle density was varied up to a weight percent of 0.014% (w/v) of rutile powder in water. Similarly, it was seen that the pumping rate was dependent on the light intensity used to irradiate the sample (Figure **2-3b**).

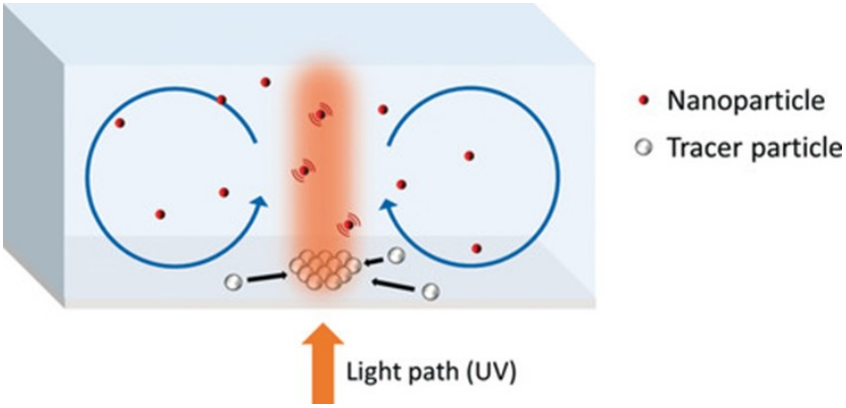

Figure 2-1: An illustration of the present system. A suspension of plasmonic nanoparticles is irradiated from below. Added tracer particles will respond to the flow. If they are allowed to settle out, they will be pressed together into colloidal crystals such as that in Figure **2-4**.

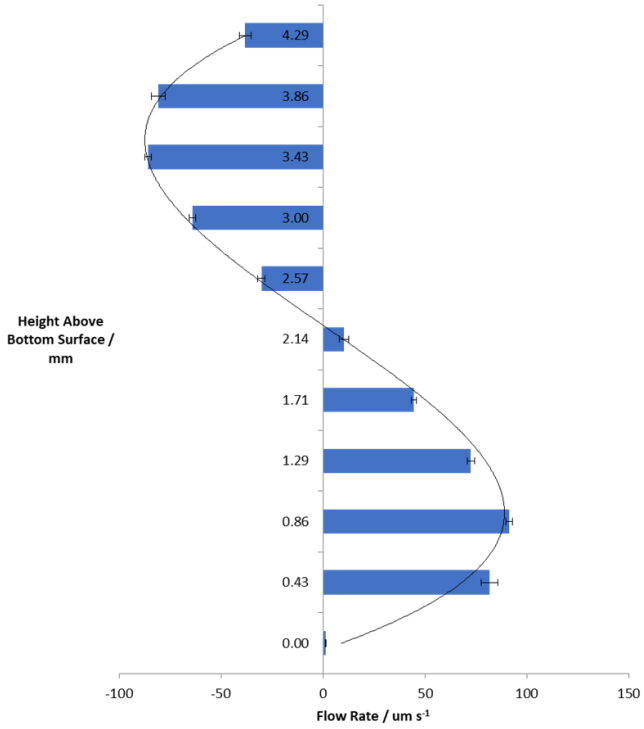

Figure 2-2: The pumping rates as a function of height above the bottom of the cell. The above S-curve is a demonstration of the convective nature of the induced flow. The measurement at the top does not return to zero since the top of the fluid is open to air contained within the chamber. For this trial, the TiO_2 (360±70 nm) concentration was set at 0.0071% w/w in water. 10 µm polystyrene tracer particles were used to observe flows. Error bars are standard deviation of the ten particles monitored at each height.

These rates were all tested at the same height of 1140 µm above the bottom surface. By testing a series of different heights within the chamber, convection was observed in the form of inward pumping near the bottom of the chamber and outward pumping near the top. This is highlighted by the s-shaped curve given in Figure **2-2** (Supporting Videos 2-1 and 2-2).

The lamp can be used to direct the location of the light spot and, therefore, the location of pumping. The convective nature of this fluid motion was further demonstrated using a glass walled cell. When the bottom of the cell was irradiated with UV light, a thread-like strand of particles was ejected from the surface and proceeded to demonstrate convective rolls on either side of the irradiated region. This can be seen in Figure **2-4** and Supporting Video 2-3.

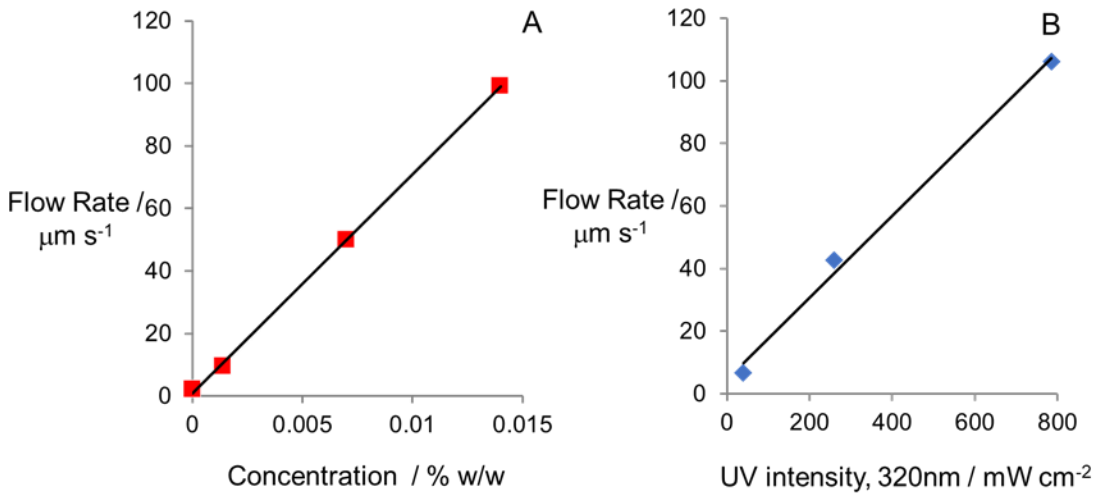

Figure **2-3**: A) The fluid flow rate towards the spot of UV irradiation as a function of weight percent of TiO_2 (360±70 nm) particles in water. Ten polystyrene tracer particles (10 µm) were tracked at each concentration. B) The flow rate also showed a linear dependence on UV light intensity. The standard deviation of each point was less than 3 µm/s.

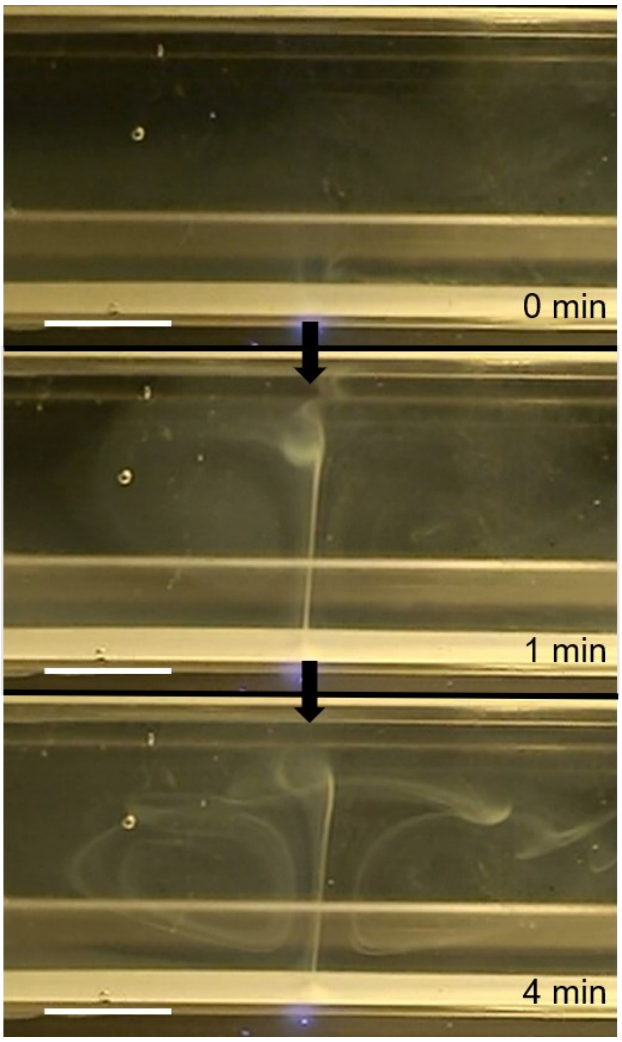

Figure **2-4**: A flat walled cell was used to visualize the convective flows arising from local particle heating. Here, a 2 mg/mL 360±70 nm TiO_2 particle suspension was allowed to settle out before being irradiated from below with ultraviolet light. The resulting fluid flows were strong enough to eject particles upwards as seen in the middle cell. This pumping proceeded to carry the particles through the characteristic loops of a bulk flow by convection. The chamber had a height of 1.2 cm and a width of 0.4 cm. It was cut to be 7 cm long. This process can be seen in Supporting Video 2-3. Scale Bar: 0.5 cm.

2.2.3 Colloidal Crystal Assembly from Light-Based Pumping

In order to demonstrate the utility of this technique, the induced flows were used to collect and organize assemblies of inert tracer particles. When tracer particles (10 μm polystyrene beads) were allowed to settle out, the flows near the bottom surface carry the particles and organize them in the irradiated area. This can be used for the active particles themselves as well as for any tracer particles that are added to the solution (Figure **2-5**). When these inward flows are sustained for about 45 min to an hour, polystyrene tracer particles are pressed together into a 2-dimensional close-packed architecture. This assembly was aided by the addition of sodium nitrate (0.14 mM) to mitigate buckling by increasing surface interactions. A demonstration of this is given in Supporting Video 2-4 within which the particles come together and then are pressed into the organized structure.

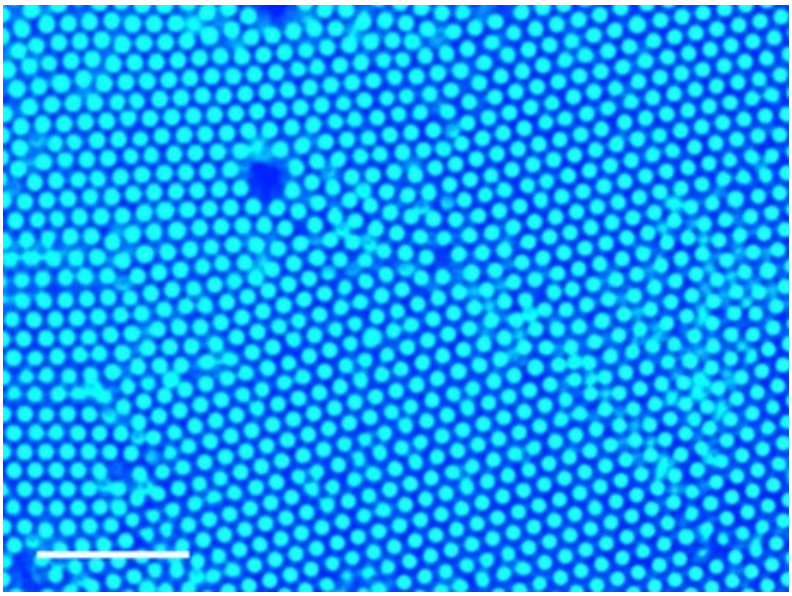

Figure **2-5**: The ensemble of 10 μm polystyrene tracer particles will take on a close-packed arrangement due to the uniform inward flow. Here, the 10 μm polystyrene tracer particles demonstrate this packing while the solution is pumped by 0.007% w/w TiO_2 (360±70 nm) in water. 20x magnification. Sodium nitrate (0.14 mM) was added to mitigate buckling. This process can be seen in Supporting Video 2-4. Scale bar: 75 μm.

Once the UV is turned off, the particles immediately begin to diffuse randomly, slowly disassembling the colloidal crystal (Figure **2-6**). If left overnight, the particles become dispersed across the bottom surface of the cell. At this point, they can be brought together again by irradiating a new region of the surface. In this way, we demonstrated the ability to reversibly collect particles anywhere within the sample chamber.

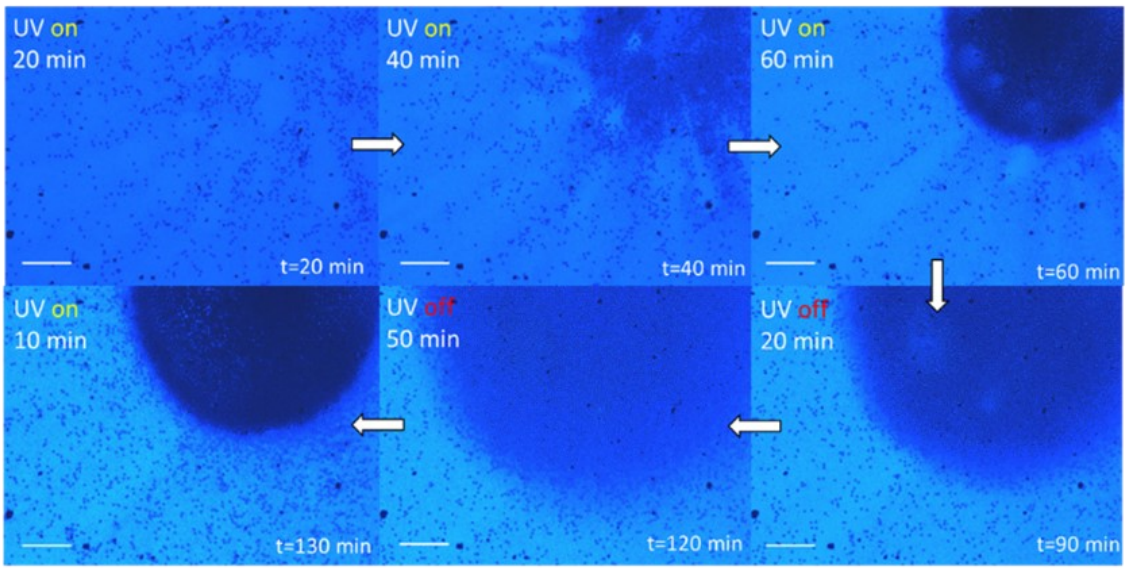

Figure **2-6**: Collection of particles (10 µm polystyrene) by inward pumping flows induced by irradiation of TiO_2 (360±70 nm, rutile) particles. Once the UV light is turned off at 70 min, the ensemble will begin to diffuse apart as seen in the fourth and fifth images. The light is then turned on again for the remaining 10 min and the particles begin to assemble again. This progression is given clockwise from the top left. 5x magnification. Scale Bar: 200 µm

2.2.3 Experiments to Test Heat-Based Mechanism

The thermal convection mechanism was confirmed by varying the surface charges and ionic strength of the medium. Sodium nitrate was added to the suspension at a concentration of 214 mM. This raised the speed somewhat, but the direction remained the same (Figure **2-7**). This rules out an ionic diffusiophoresis or electroosmotic mechanism for which the velocity should decrease with increasing ionic strength of the medium.[13,21] To supplement these results, cationic amino-polystyrene particles (6 μm, Polysciences) were used as tracers and the solution was adjusted to a pH of 2 using hydrochloric acid. With the tracer particle zeta potential now increased to 18±6 mV compared to -50±3 mV for the unfunctionalized particles, the direction of flow remained unchanged (Figure **2-7**), again demonstrating that the observed fluid flows are charge independent.

Given the above results, follow-up experiments were performed using hexadecane as the medium in place of water. The titanium dioxide particles were found to aggregate significantly, and the addition of tracer particles was unnecessary to observe the flows. Once again, inward flows were promoted upon UV irradiation. As with the above trials, the ability to pump under these conditions further indicates the charge and ion gradient independence of the pumping behavior. At a TiO_2 concentration of 0.007% w/v, flows were observed in hexadecane at 29±3 μm/s as opposed to the 50±3 μm/s observed in water (Figure **2-7**). This decrease is attributed to the difference in viscosity between the two solvents. At 298.15 K, hexadecane has a dynamic viscosity of over three times that of water at 3.01 mPa·s and 0.89 mPa·s, respectively. To our knowledge this is the first demonstration of light-driven fluid pumping in organic medium.

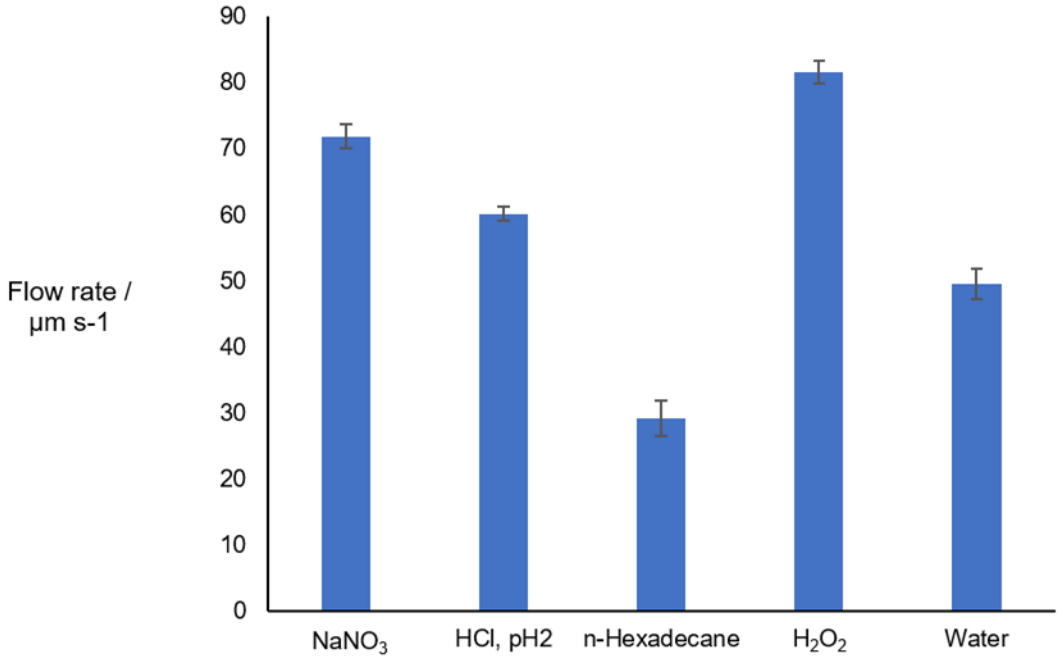

Figure 2-7: Pumping rates of fluid under different conditions. Each trial involved 0.0071% w/w TiO_2 (360±70 nm, rutile) particles. Rates were observed by using 10 µm polystyrene tracer particles for each of these trials except for n-hexadecane, for which the TiO_2 aggregation was significant enough for it to serve as its own tracer. The medium effects the pumping rate; however, the particles will generate pumping in any fluid. The high ionic strength trial (NaNO3, 214 mM) indicates that pumping will occur independent of any ion gradients present. For the low pH trial, the zeta potential was positive (18 mV up from -50 mV, adjusted using HCl). Therefore, the pumping direction is independent of surface charges. Given these points, it is of little surprise that pumping was also observed in n-hexadecane. The velocity drop-off is attributed to the higher viscosity of n-hexadecane. Hydrogen peroxide (1.5%) was added to test how a reactive species would influence the pumping behavior. The higher rate appears to be indicative of its exothermic decomposition and perhaps an expansion due to the higher number of products than reactants. For each of these trials, the pumping was measured at 1140 µm above the bottom surface.

For comparison to these active particle suspensions, a patch of TiO_2 was fabricated (Section 2.2.4) and tested for its ability to generate flows. While UV light was directed towards the cell and away from the patch, flows were not observed. The light was then shifted over to the patch and flows immediately began in the region being irradiated. This is shown in Supporting Video 2-5. The patch was 100 nm thick, suggesting that even thin layers were sufficient to generate pumping at a modest rate.

To confirm that the particles were generating heat, a k-type thermocouple was inserted in the solution during UV irradiation. After increasing rapidly, a sustained temperature increase of 0.6-0.8 K was observed for TiO_2 (0.014% w/v, 360±70 nm). (Figure **2-8**). Since the pumping is attributed to local heating, it is important to note that this migration is not due to thermophoresis. First, the Soret constant is usually positive, indicating that particles would move from the hot towards the cold regions.[11,12] The inward flows near the bottom would therefore be unexpected. The bulk fluid flow is also contrary to thermophoretic motion.

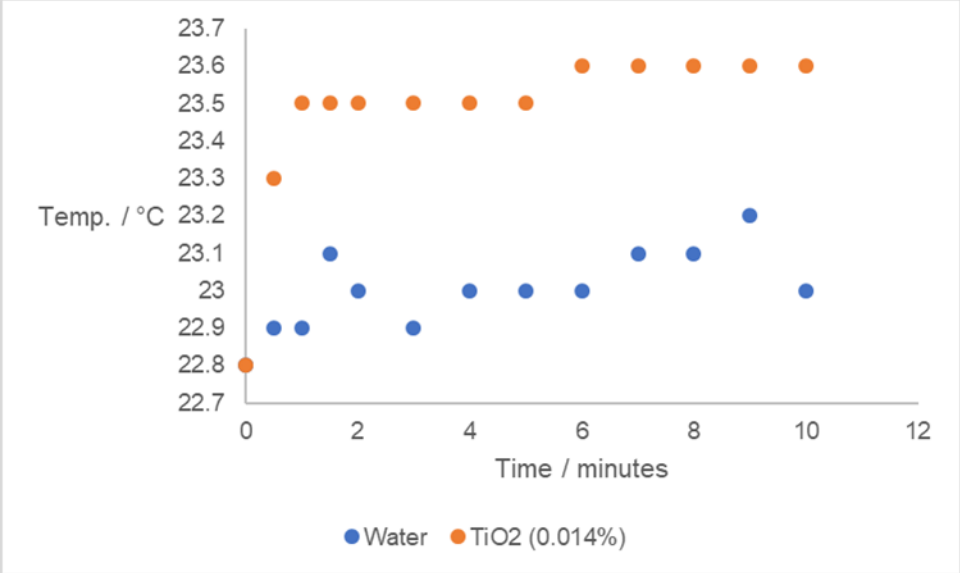

Figure 2-8: A temperature increase of 0.6-0.8 K was observed when a suspension of TiO_2 particles (360±70 nm, 0.014%) was irradiated with UV light. This was performed using a k-type thermocouple (Omega) set in the center of the cell with the top removed. The baseline was corrected for the starting temperature. Each sample was allowed to equilibrate for 10 minutes before being irradiated.

2.2.4 Experimental Results Using Gold Nanoparticles

Gold nanoparticles (21±5 nm) were also found to work well in promoting light-powered fluid flows (Figure **2-9**). It is known that such particles in water will yield substantial amount of heat when irradiated at their plasmon resonance wavelength.[22] This heat energy rapidly dissipates into the surrounding solution. In our system, a flow rate of 179 µm/s is reached at 0.0001% w/v of gold in solution. By comparison, 0.014% w/v TiO_2 (360±70 nm) yielded a flow rate of about 100 µm/s. This gold nanoparticle-based pumping system also demonstrates an increase in pumping rate with increasing particle concentration (Figure **2-9**).

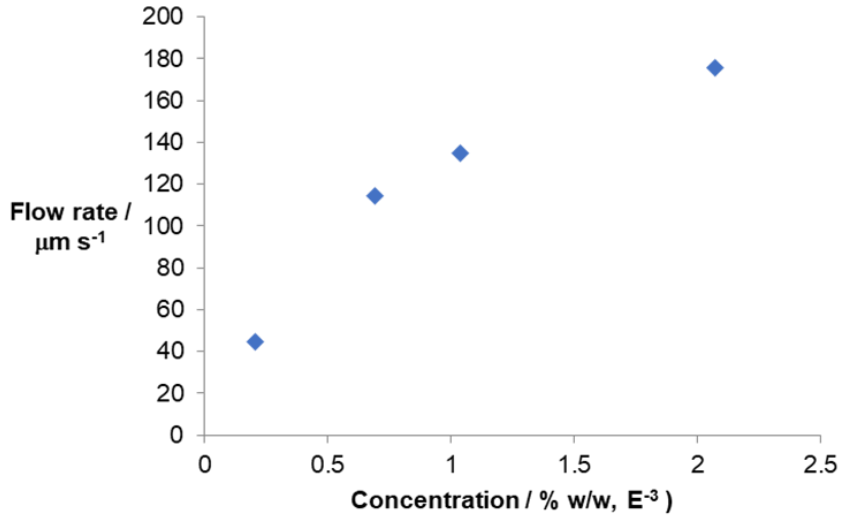

Figure **2-9**: The flow rate as a function of concentration of gold nanoparticles (21±5 nm) added. The flow rates were considerably higher for these trials. Compared to 0.014% w/w TiO_2 (360±70 nm), gold demonstrates an 80% rate increase while still using less than 15% of the weight percent needed of TiO_2. The linearity appears to fall off at higher concentrations of gold. The standard deviation for each point was less than 3 µm/s.

On account of its much lower rate of aggregation, gold can be used to promote migration of tracer particle assemblies. When the irradiated region was shifted, the ensemble collectively migrated to the new location. An example of this is given in Figure **2-10** (Supporting Video 2-6). Large sections of the ensemble retain their colloidal crystal architecture as this transition occur, while grain boundaries will form and anneal within the lattice structure

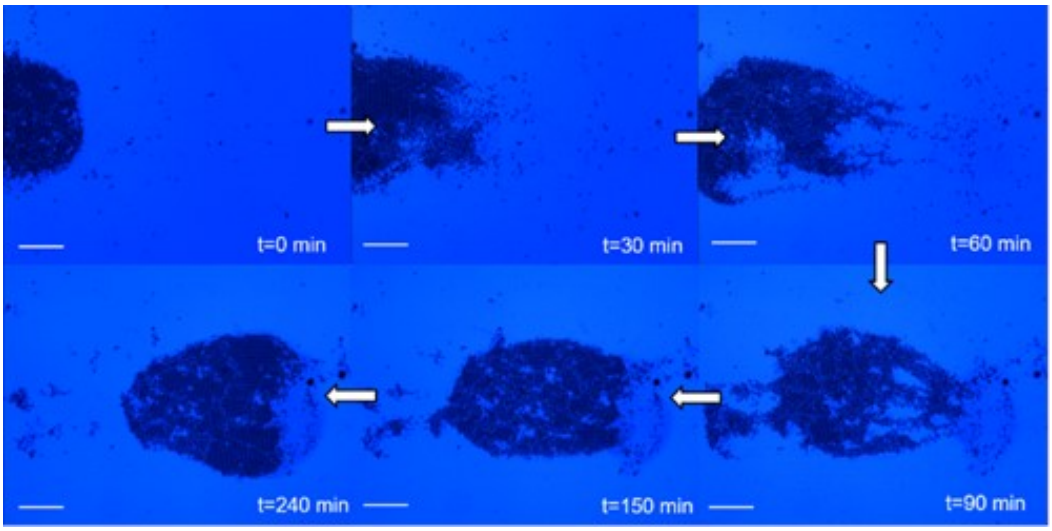

Figure **2-10**: Migration of tracer particle (10 µm PS) cluster due to flows produced by heating gold nanoparticles (21±5 nm). The ensemble of tracer particles was allowed to gather before the light was aimed elsewhere in the chamber. Here the light source and the window were moved to the right of where the particles were initially gathered (seen at left in the first frame). The light was shifted to the right by about 1500 µm and the particles were seen to move towards the new location. The images are arranged clockwise from top-left. 5x magnification. Scale bar: 200 µm. Also given as Supporting Video 2-6.

2.3 Experimental

2.3.1 Particle-Based Pumping Set-Up

These trials were performed in a cylindrical steel chamber (d = 1 cm, h = 0.8 cm) so that the medium could be varied without dissolving the walls (Figure **2-11**). Cover slips were affixed to the top and the bottom of the cell such that the solution could be observed. 360±70 nm titanium dioxide (rutile) particles were used as purchased (US nanomaterials). The dimensions were tested using scanning electron microscopy and the crystal structure was confirmed to be rutile by powder x-ray diffraction. In a typical experiment, the amount of TiO_2 was varied but the 10 μm polystyrene-latex tracer particles (Polysciences) were kept at 0.0064% (w/v) and used to observe the motion of fluid within the steel-walled sample chamber. For the 3D collection trials, the concentration was increased to 0.025% (w/w) in order to induce buckling. 6 μm amino-polystyrene particles (Polysciences) were used for trials to assess the effect of particle surface charge. The surface charge was determined using a Malvern Zetasizer nano ZS. For all trials, the samples were sonicated for 1 min and then vortexed again immediately before being added to the steel chamber and observed. 350 μl of solution were used for each trial, meaning that the top of the chamber was filled with air between the solution and the cover. In between each trial, the steel chamber was allowed to rest on the benchtop for about 10 min in order to equilibrate with the temperature of the room. A small amount of sodium nitrate (0.14 mM) was added to the collection trial to slightly mitigate buckling (Figure **2-5**). By increasing the repulsion between the particles and the surface, the number of particles pressed out of the layer is believed to have decreased. The samples were observed on a Zeiss Axiovert 200 MAT microscope using a Point Grey Flea2 camera on a 5x objective. Unless stated otherwise, videos were recorded at 1140 μm above the bottom surface, about a quarter of the total height of solution. For all experiments, a HAL 100 mercury arc lamp was used as a light source and a UV filter was used in order to lower the light intensity to roughly

32 mW/cm2 recorded at 320 nm. The irradiation spot had a diameter of 2 mm surrounded by a 2 cm ring of noticeably lower intensity. The intensity was read by a 1 cm diameter light meter, thus making our effective intensity about 785 mW/cm2 approximating for the 2 mm spot. The incident light was limited to the 300-400 nm range. The light intensity trials were performed using additional 1.3 and 0.6 optical density filters.

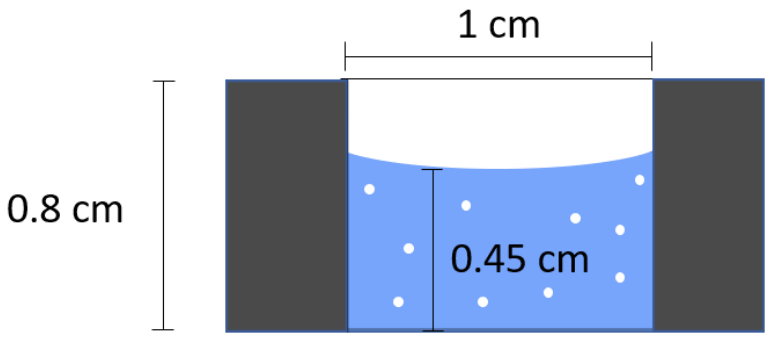

Figure **2-11**: Schematic of the experimental set-up. A cylindrical steel chamber was prepared with glass cover slips on top and bottom to contain solution. A suspension of plasmonic nanoparticles was added to a chamber. The type of particle and concentration were varied for different experiments and the same chamber was washed and re-used throughout the course of the project.

2.3.2 Particle Tracking and 3D Collection Trials

Particle tracking was performed manually using Tracker software. The flow rate of each particle was determined as the particle moved in-plane at a distance around 1400 μm away from the flow center. This was done for consistency and since the particles would begin to move in the z-direction at the expense of their in-plane velocity as they approached the center. Unless stated otherwise, the velocity in all trials was measured at one quarter of the solution height (1.125 mm), where the maximum flow rates were observed.

In order to observe 3D collection, a suspension of 0.014% w/v TiO_2 (360±70 nm) was mixed with 0.025% w/v of 10 μm polystyrene beads. This was allowed to rest overnight while under irradiation until the water had completely evaporated, leaving a mound of polystyrene beads in the targeted area. The cover slip was then observed from above using a Zeiss AxioZoom V16. The cover slip was assigned as height = 0 and the highest point of the mound was focused on and measured at a height of 88 μm.

2.3.3 Gold Nanoparticle Synthesis

The synthesis of Au NPs was performed using a borohydride reduction method as described by Zhao and Bernd.[23] 5 ml of 0.001 M HAuCl4 solution was mixed with 5 ml of 0.005 M trisodium citrate (Na3C6H5O7) in a 50 ml beaker and the reaction mixture was subjected to vigorous stirring and placed in an ice bath to maintain a temperature of ~4 °C. After 5 min, 0.01 M of ice-cold NaBH4 solution was added dropwise to the reaction mixture while stirring. The reaction progress could be monitored by a change in color of the solution from colorless to pink immediately after the addition of NaBH4, and finally to a deep red after about 10 min. The wine-red color Au NPs exhibited a plasmon band at 536 nm (from UV-Vis data) and their sizes were 21±5 nm as obtained from DLS experiments (Malvern Zetasizer nano ZS). The as prepared Au nanoparticles were stored below 10 °C for future studies. A TEM image of the as-synthesized Au nanoparticles is shown in Figure **2-12**.

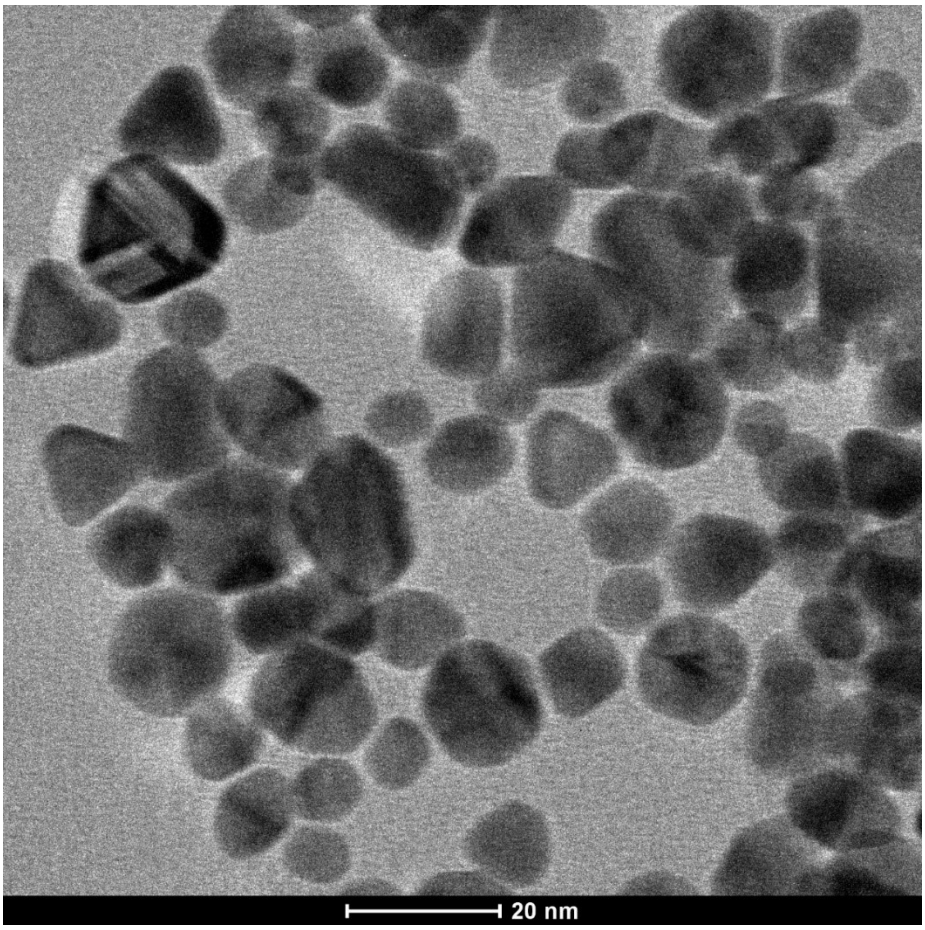

Figure **2-12** Transmission electron microscope (TEM) image of the synthesized gold nanoparticles. This was performed using a Tecnai G2 20 XTWIN TEM.

2.3.4 Preparation of TiO_2 Patch and Experiment

The 3 mm TiO_2 patch was created using a Kurt J Lesker Lab-18 E-beam deposition system. A mask was prepared using a sheet of aluminum foil and a 3mm hole which was then wrapped around a circular glass cover slip. 100 nm of TiO_2 was deposited at 1 Å/s. TiO_2 set securely onto the glass without the need of an adhesive layer. The coverslip was then used as prepared as the bottom surface in the steel-walled cell.

2.3.5 Flat-Wall Cell Preparation

In order to observe the convective motion from the side, a glass-walled cell was assembled. 1.2 cm by 0.4 cm rectangular glass tubing was purchased from Vitrocom. A 7 cm length was broken off and affixed to a glass microscope slide using commercial superglue, taking care to keep glue out of the area that would later be irradiated with UV light. The ends were capped with broken microscope slides, but with a small hole to allow for the addition and removal of solution. The trial can be seen in Supporting Video 2-3.

2.4 Conclusion

In conclusion, we have demonstrated a method of producing highly controllable flows that can be utilized to collect particles around a point source. TiO2 and gold particles serve as models for the technique, which can be performed without any preassembly, requiring only that care be taken in monitoring either the light intensity or the light-active particle concentration. The ability to locally concentrate inactive tracers can extend across many different media, easily gathering plastic particles. By this method, one should be able to concentrate bacteria and other cells with the same level of ease. This technique can be used in any medium that does not react with the active particle or under UV irradiation. For the above reasons, this particle-based, light-driven flow technique is a powerful new addition to the toolbox of active matter induced dynamic assembly strategies.

2.5 Acknowledgements

I would like to thank the Materials Research Institute at Penn State for the use of their facilities and for their useful insight. Thanks are also due to Josh Kauffman and Subhadip Ghosh for collecting SEM data and providing gold particles, respectively. This work was made possible by NSF-CCI Award Number 1740630. Any opinions, findings, and conclusions or recommendations expressed in this chapter are those of the author and do not necessarily reflect the views of the National Science Foundation.

2.6 References

[1] W. F. Paxton, K. C. Kistler, C. C. Olmeda, A. Sen, S. K. St. Angelo, Y. Cao, T. E. Mallouk, P. E. Lammert, V. H. Crespi, *J. Am. Chem. Soc.* **2004**, *126*, 13424–13431.

[2] S. Sanchez, L. Soler, J. Katuri, *Angew. Chemie - Int. Ed.* **2015**, *54*, 1414–1444.

[3] F. Wong, K. K. Dey, A. Sen, *Annu. Rev. Mater. Res.* **2016**, *46*, 407–432.

[4] P. Illien, R. Golestanian, A. Sen, *Chem. Soc. Rev.* **2017**, *46*, 5508–5518.

[5] Y. Tu, F. Peng, D. A. Wilson, *Adv. Mater.* **2017**, *29*, 1–20.

[6] C. Zhou, H. Zhang, Z. Li, W. Wang, *Lab Chip* **2016**, *16*, 1797–1811.

[7] F. Wong, A. Sen, *ACS Nano* **2016**, *10*, 7172–7179.

[8] S. Das, O. E. Shklyaev, A. Altemose, H. Shum, I. Ortiz-Rivera, L. Valdez, T. E. Mallouk, A. C. Balazs, A. Sen, *Nat. Commun.* **2017**, *8*, 1–10.

[9] S. Sengupta, D. Patra, I. Ortiz-Rivera, A. Agrawal, S. Shklyaev, K. K. Dey, U. Córdova-Figueroa, T. E. Mallouk, A. Sen, *Nat. Chem.* **2014**, *6*, 415–422.

[10] M. Li, Y. Su, H. Zhang, B. Dong, Nano Res. **2017**

[11] J. S. Donner, G. Baffou, D. McCloskey, R. Quidant, *ACS Nano* **2011**, *5*, 5457–5462.

[12] D. P. Singh, U. Choudhury, P. Fischer, A. G. Mark, *Adv. Mater.* **2017**, *29*, 1–7.

[13] Y. Hong, M. Diaz, U. M. Córdova-Figueroa, A. Sen, *Adv. Funct. Mater.* **2010**, *20*, 1568–1576.

[14] M. T. Carlson, T. S. Barton, P. J. Tandler, H. H. Richardson, A. O. Govorov, *Mater. Res. Soc. Symp. Proc.* **2009**, *1172*

[15] B. J. Zhang, Y. Li, X. Zhang, B. Yang, *Adv. Mater.* **2010**, *22*, 4249–4269.

[16] B. O. D. Velev, E. W. Kaler, *Adv. Mater.* **2000**, *12*, 531–534.

[17] N. M. Dimitriou, G. Tsekenis, E. C. Balanikas, A. Pavlopoulou, M. Mitsiogianni, T. Mantso, G. Pashos, A. G. Boudouvis, I. N. Lykakis, G. Tsigaridas, M. I. Panayiotidis, V. Yannopapas, A. G. Georgakilas, *Pharmacol. Ther.* **2017**, *178*, 1–17.

[18] K. M. Haas, B. J. Lear, *Chem. Sci.* **2015**, *6*, 6462–6467.

[19] X. Huang, M. A. El-Sayed, *J. Adv. Res.* **2010**, *1*, 13–28.

[20] M. L. Brongersma, N. J. Halas, P. Nordlander, *Nat. Nanotechnol.* **2015**, *10*, 25–34.

[21] T. R. Kline, W. F. Paxton, Y. Wang, D. Velegol, T. E. Mallouk, A. Sen, *J. Am. Chem. Soc.* **2005**, *127*, 17150–17151.

[22] A. O. Govorov, W. Zhang, T. Skeini, H. Richardson, J. Lee, N. A. Kotov, *Nanoscale Res. Lett.* **2006**, *1*, 84–90.

[23] J. Zhao, F. Bernd, *Proceedings of the Nanocon*, Brno, Czech Republic, **2015**, 597-604

Chapter 3

Optimization of Metallic Nanoparticles for Photothermal Convective Pumping and Assembly Behavior

The work in this chapter is a modified version of a manuscript in preparation adapted from Kauffman, J.K; Tansi, B.T.; LaSalle, C.; Manna, R.K.; Shklyaev, O.L.; Balazs, A.; Sen, A. Investigation of colloidal assembly under convective flows and on inclines. In Preparation

A recent investigation has demonstrated the use of photothermally generated convective flows as a self-assembly method. This result introduced a need for more robust investigations of particle type and chamber geometry in order to better realize the nascent potential of such a system. This investigation specifically addresses the effect of nanoparticle size and composition for pumping driven by ultraviolet light. Self-assembly and diagnostic tests can generally be performed without concern for the wavelength considered. The vast body of photothermal work considers the plasmon resonance wavelength and near infrared light. Meanwhile, UV light can be a fitting choice for many applications as it is a high energy light source. We go on to use some of these particles in order to address unique capabilities in active self-assembly and microparticle separations based on size. This chapter specifically outlines experimental results. A computational complement to the assembly and separation work can be found in Ref. 26.

3.1 Introduction

Chemical micropumps have been increasingly studied due to their ability to move fluid in confined environments. Such systems have potential in areas ranging from biomedicine and drug delivery to self-assembly applications. Regarding biomedicine, changes within the body could be used to selectively release therapeutic agents. In a recent example, the leaching of insulin from a gel matrix could be modulated depending on changes in glucose levels.[1] Similarly, these pumps can act as sensors for toxin detection at parts per billion concentrations using enzymes and their catalytic inhibitors.[2] In recent years, the number of possible reagents and mechanisms has been steadily growing[3,4] due to the promise for such applications. Generally, this induced-flow principle can be used to detect the presence and concentration of anything for which the reaction rate, and therefore fluid velocity, is dependent. To take these techniques further, it pays to build the catalog of possible pumping methods. For the most part, such micropumps rely on a pre-fabricated region with catalytic activity. The catalysis either stems from the property of the material or else the activity of surface bound components such as enzymes that will generate fluid motion through the reaction with their specific substrate.[1,2,5] These are largely based on phoretic effects arising from local ion exchange or production,[6–9] or else heat generation,[1] which will create density gradients within solution.

The use of such pumping in self-assembly methods has also been explored, but the utility is somewhat muted by the requirement for pre-fabrication. First, the pump is not reconfigurable within the system. Once bound, the location of the pump cannot be changed without disassembly and the patch may disrupt colloidal crystal formation. These systems also require the input of a reactant to maintain the fluid convection within the system. Once the chemical runs out, the system stops pumping and once introduced, pumping cannot be stopped until the reaction is fully completed. A recent report outlines a pumping method that uses light to prevent these limitations.[10]

Via the photothermal effect, metal nanoparticles under ultraviolet (UV) light irradiation will yield substantial heating,[11–16] which can translate to rapid fluid motion by convection.[17] High spatiotemporal control can be attained by simply shifting the irradiated area or by varying the light intensity. In this communication, we seek to expand on the initial system by probing size and composition effects of metal nanoparticles. We go on to demonstrate that convective flows can be used to separate particles based on size.

3.2 Results and Discussion

3.2.1 Effect of Size for Gold and Silver Nanoparticles

Metal nanoparticles exhibit several pronounced size-dependent properties, particularly regarding catalysis[18–20] and interactions with light. Regarding light, the wavelength and intensity of both absorbed and emitted light can be carefully tuned. When the energy taken up from incident light is significantly greater than that which is emitted, the excess energy is typically released as heat. This "photothermal effect" has been increasingly studied in recent years due to efforts to exploit it for tumor ablation.[13,21,22] This phenomenon is well documented for particles irradiated at their surface plasmon resonance (SPR) wavelength (usually 515-632 for gold) as well as within the therapeutic near-infrared window.[23] However, for ex vivo diagnostics and self-assembly applications, higher energy light is permissible.

Increasing particle size has been seen to correlate with decreasing light-to-heat conversion efficiency. However, the absorption cross section has been seen to increase with size.[11,24] Specifically, smaller particles lose less energy in the form of fluorescence, however larger particles absorb disproportionately more light in relation to their increased size. As such, an increase in size

should lead to a commensurate increase in pumping velocity due to greater heat generation. As shown in Figure 3-1A, this appeared to hold true up to a particle size of 80 nm in diameter before falling off. This likely indicates that the increasing light absorption fails to compensate for the decreasing conversion efficiency at particle sizes above a certain threshold.

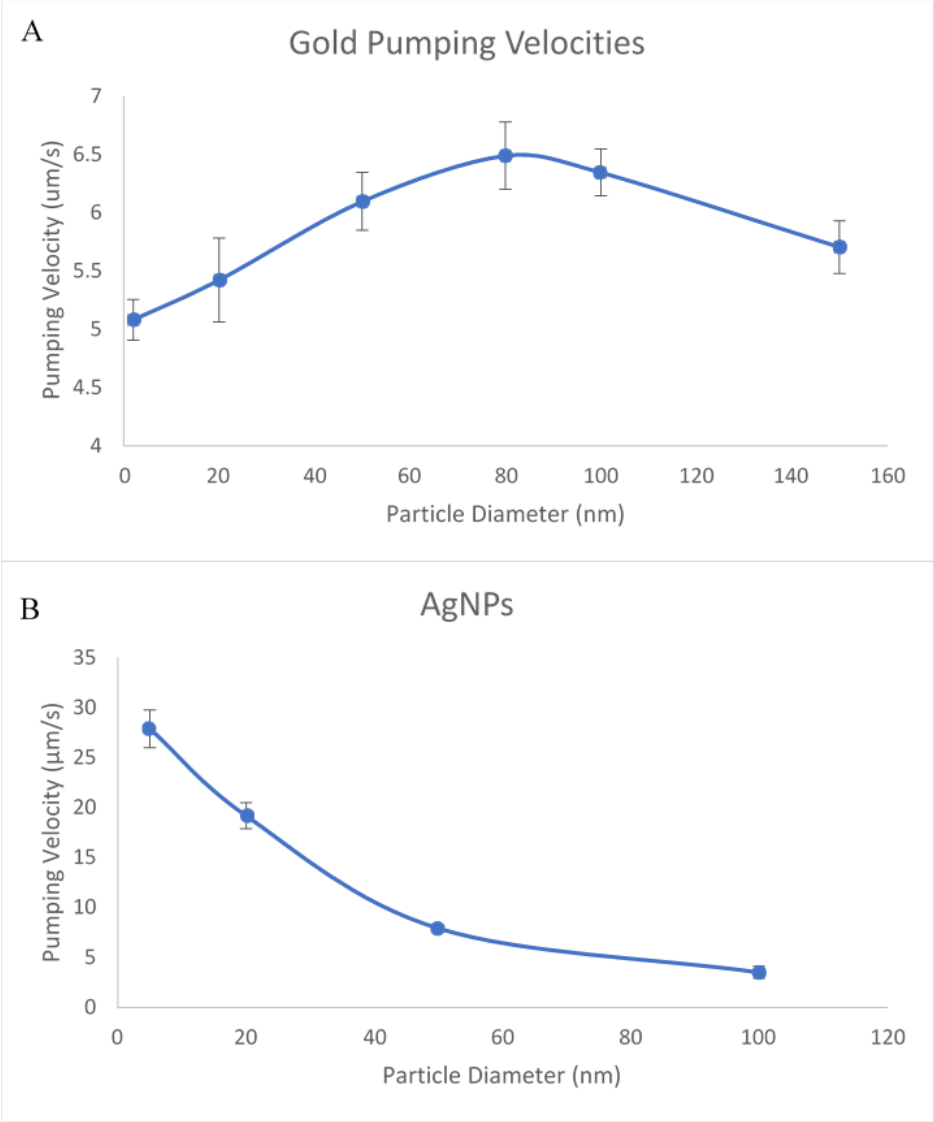

Figure **3-1**: Plots showing the fluid velocity from thermal convection of gold (**A**) and silver (**B**) nanoparticles of various sizes during irradiation with UV light. The weight percents were kept the same for all samples. For both experiments, ten carboxylate capped polystyrene particles were tracked for ten steps to obtain all data points. All solution contained 0.001% w/w of the plasmonic nanoparticle with 3 µm polystyrene tracers (0.0025%w/w) for flow observation. 10 particles were tracked for each datapoint. Errors bars are the standard deviations.

While AuNPs exhibit a plasmon wavelength above 500 nm, silver nanoparticles have this band in the near UV at small particle sizes. Therefore, the ultimate heating effect and pumping velocities should be considerably higher using smaller particles, directly contrasting with gold under the same conditions. As given in Figure 3-1B, silver nanoparticles will promote steadily lower flow rates as the particle size is increased. This is in line with the plasmon band slowly shifting away. Tested AgNPs were sized at 5, 20, 50 and 100 nm with SPR wavelength moving farther away from the UV range as size increased, for which we see λ_{max} values in the range of 393-482 nm.

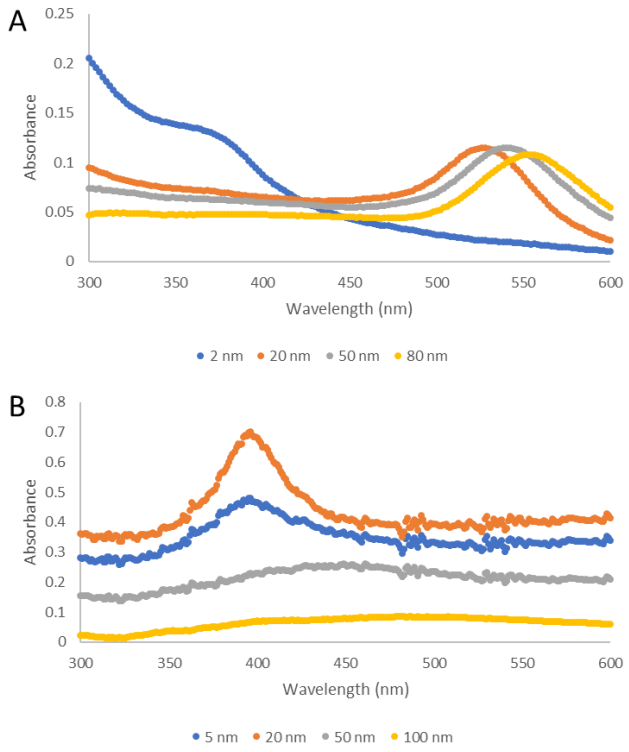

Figure 3-2: The UV-vis absorption spectra for different sizes of gold (A) and silver (B) nanoparticles.

Experimentally, we observed that 5 and 20 nm particles generate much higher pumping rates than the other two sizes. The 5 nm NPs have an SPR wavelength around 390 nm which falls into the range emitted by the lamp used in these trials. This results in extremely high light absorption and subsequent heat generation. The absorbance spectrum for 20 nm particles closely overlaps that of the 5 nm (Figure **3-2**), however the degree of absorption was significantly higher, which is contrary to our finding that the pumping rate is lower. We attribute the lower pumping velocity to the ratio of scattered to absorbed light, which is known to increase as the particle size increases.[25] This has been demonstrated for gold nanoparticles and could reasonably be expected of silver as well.

3.2.2 Convection-Driven Migration Rates of Particles Along Surfaces

Convective flows and reconfigurable pumping are not the only unique characteristics observed in this system. Surprisingly, the surface migration rates of larger tracer particles are higher than that of smaller ones. By most ion-based phoretic mechanisms, smaller particles will move faster due to the higher ratio of surface charge to fluid drag. In this instance, the fluid drag is effectively pushing the particle. Larger tracer particles on the bottom surface are exposed to higher fluid velocities owing to the distance that they extend from the wall. Figure **3-4** highlights this principle by considering the near-surface profile of the convective S-curve given in Figure **3-3**. Three tracer particle sizes (3, 10, and 20 μm) were introduced to the system simultaneously and their rates were monitored and compared. As seen in Figure **3-5** and Supporting Video 3-1, the largest particles move the fastest as they are influenced by the higher flow rates further from the wall.

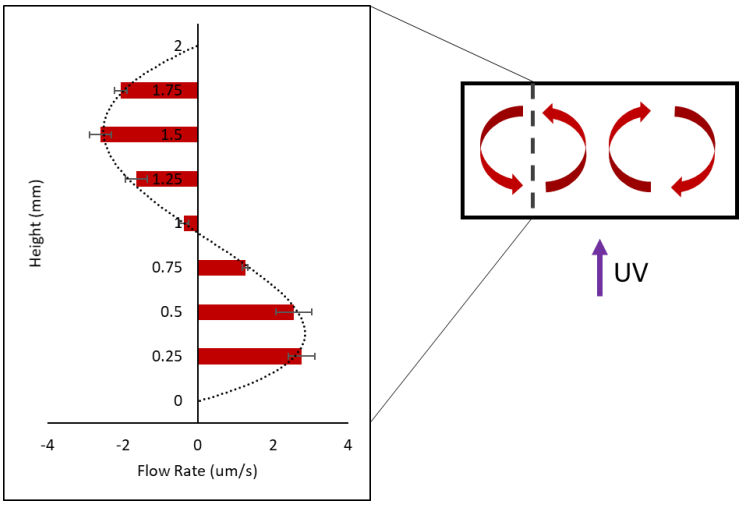

Figure 3-3: The characteristic S-shaped flow profile away from the flow center. Positive values denote inward pumping towards the irradiation point. The maximum flow velocities are seen near one quarter and three quarters of the total height. Error bars are the standard deviation. The dotted line is added to clearly display the profile.

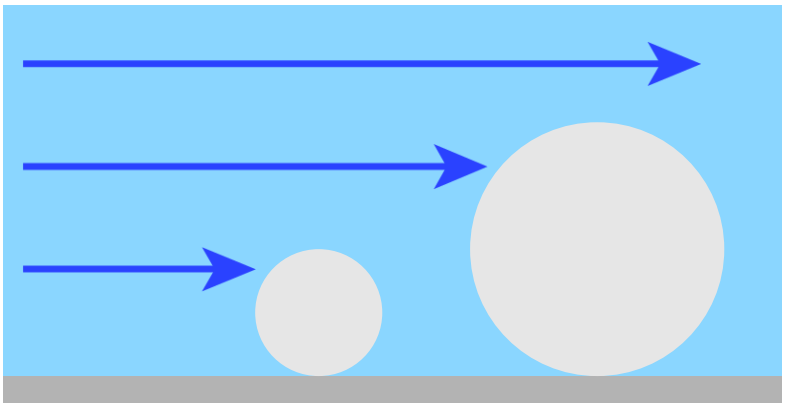

Figure **3-4**: A schematic illustrating the effect of convective flows on tracer particles at the bottom surface. The flow velocity close to the surface approaches zero. Larger particles will therefore experience higher flow rates as they protrude farther above the surface than smaller particles.

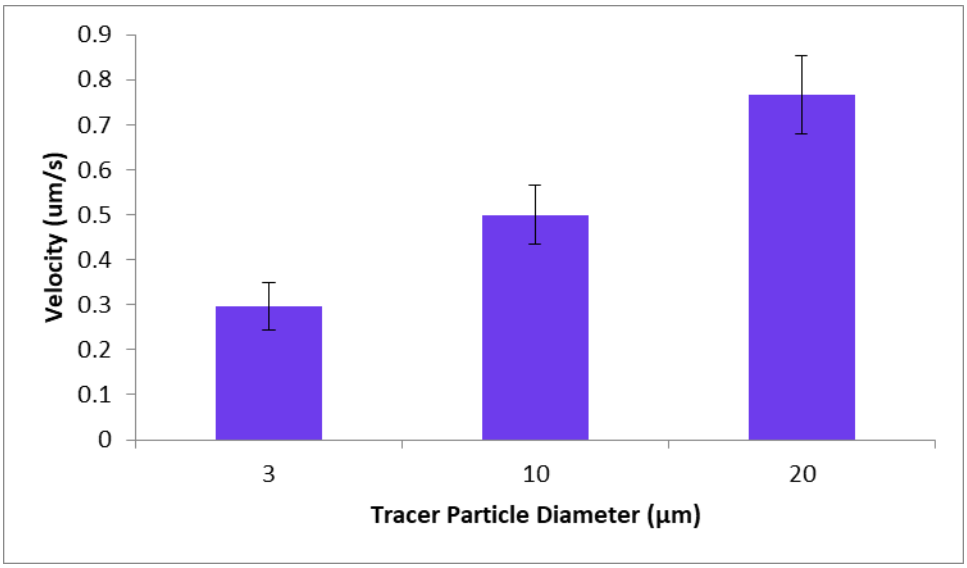

Figure **3-5**: The surface velocities of particles along the surface. Larger Particles are seen to migrate faster. These rates were measured at about 715 µm from the flow center. 5 nm AgNPs (0.0011% w/w) were used in this trial. This phenomenon can be seen in Supporting Video 3-1.

As demonstrated previously in the literature, colloidal crystal assembly is possible using convective flows using plasmonic nanoparticles.[9,10] Owing to the different rates as described above, smaller particles in this system will arrive later and a tracer particle size gradient develops over time. An example of this phenomenon is provided in Figure **3-6**, within which the flow center was fixed to the bottom right portion of the frame.

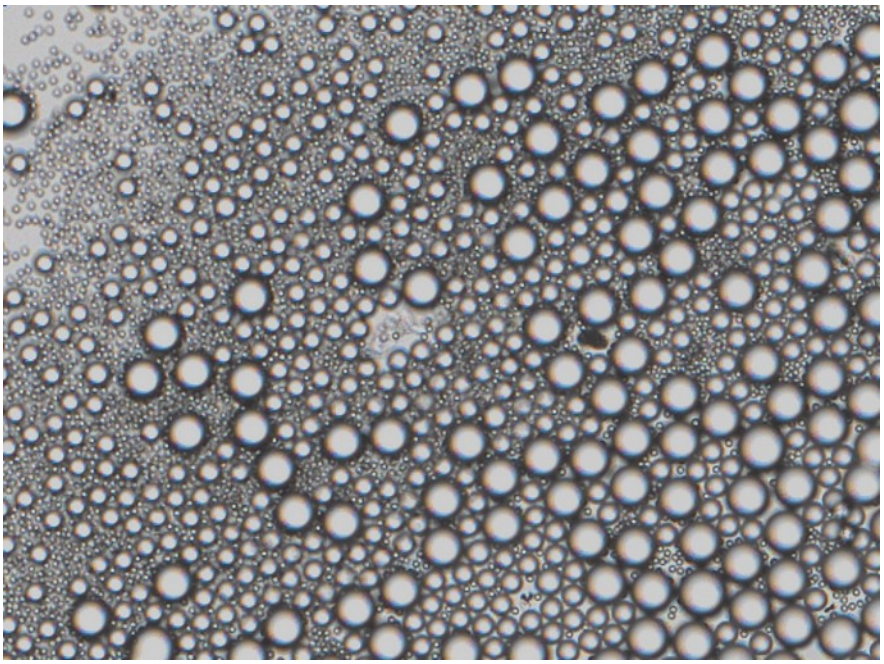

Figure **3-6**: Collection of different sizes of tracer particles on a flat surface in a solution of Ag NPs (0.011% w/w). Here, carboxylate functionalized polystyrene tracer particles of 3, 10, and 20 μm were used. Larger particles are focused towards the center of the cluster as they experience higher convective flows in the system. Pockets of hexagonal close-packed crystal structures can be observed, especially for the middle-sized 10 μm particles. The bottom of the frame is 384.8 μm across.

3.2.3 Convective Separation in an Inclined Chamber

The above example yields a crude separation of particles; however, the degree of separation can be improved considerably. Manna et al.[26] had predicted that particles will settle out to different heights when biased on an incline. By the competing effects of gravity and fluid drag, particles will settle out to a height where the two factors cancel out. Herein, an experimental complement is provided.

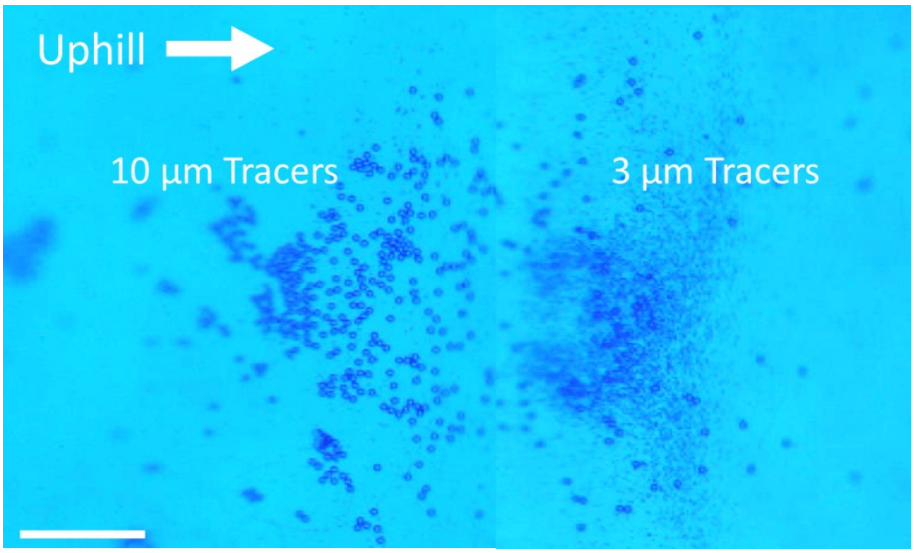

Figure **3-7**: An image showing the separation of tracer particles by size using convective flows in a 12° incline. Under convective flow, 3 µm and 10 µm tracer particles will settle out to the height at which their motion from fluid drag matches their settling rate. AuNPs 0.055% (w/w) 29 nm were used in this experiment. The scale bar is 200 µm.

A 1 mL solution was prepared containing 0.055 % (w/w) of 29 nm AuNPs and roughly 0.005% (w/w) each of 3 µm and 10 µm carboxylate-functionalized polystyrene particles. The tracer particles were seen to separate according to their size with the larger tracer particles settling further down the incline (Figure **3-2**). Although the effect of gravity is uniform everywhere, the flow rate in the chamber is dependent on the radial distance from the irradiation point. Figure **3-8** captures this effect for a single particle on a flat surface. Notably, the larger particles settle further from the flow center, despite the increased migration rate observed on flat surfaces. This stems from the relation between size and settling rate as described by Stokes law.[27]

$$U = \frac{2a^2(\rho_p - \rho)g}{9\eta} \tag{3.1}$$

Here, U is the settling velocity, a is the particle radius, ρ_p and ρ are the densities of the particle and the medium, respectively, g is the acceleration due to gravity, and η is the viscosity.

As the settling rate responds to the square of the radius, the larger particles require a stronger opposing flow rate in order to match their settling velocity. We would reasonably expect particles of identical sizes to separate based on density as well. Larger particles will sometimes become trapped in a bed of smaller particles, which can be alleviated by moving the irradiation point uphill incrementally. It is also of note that the flow center becomes shifted downhill somewhat do to the effect of gravity.[26] Upon turning off the light, the particles will settle to the bottom of the cell. The angle of the incline factors into the magnitude of the settling velocity predictably, but this angle also effects the induced flow profile. Ref. 26 includes a more thorough theoretical investigation of these effects.

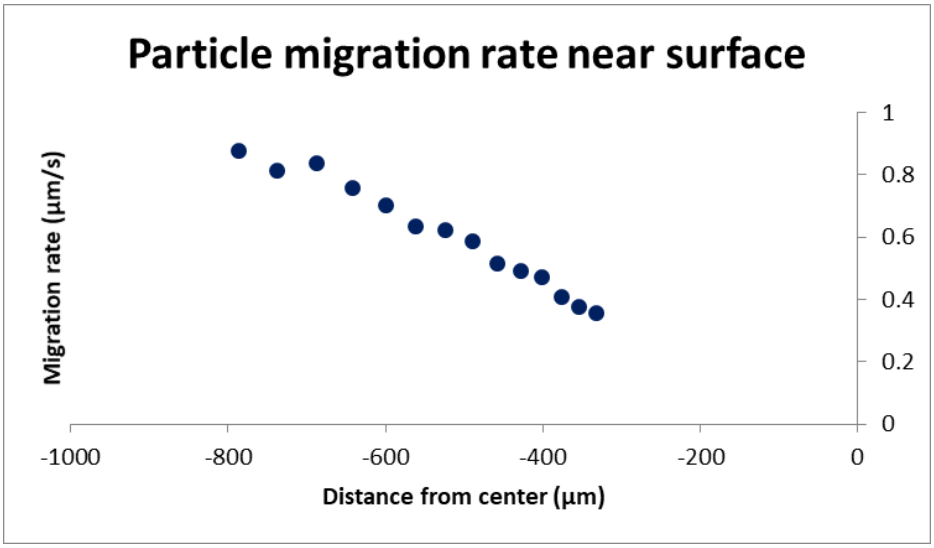

Figure **3-8**: The particle migration rate along a surface under convective flows as a function of distance from the irradiation spot. A single particle was followed over time and the rate was seen to steadily drop as it approached the center. In the incline trials, this change is responsible for particles settling out to different heights. It also demonstrates the need for a consistent radius when comparing particle types.

3.3 Experimental

3.3.1 Convective Pumping Rate Based on Particle Size and Type

Citrate-capped gold nanoparticles (AuNPs) were purchased from Nanocs Inc (2 nm, USA), and Sigma (20, 50, 80, 100, 150 nm, USA). Silver nanoparticles (AgNPs) were purchased from Nanocs (5 and 50 nm) and Sigma (20 and 100 nm). Particles were used as purchased for all experiments. Aqueous solutions of 0.001% (w/w) nanoparticles were prepared with 0.005% (w/w) of 3 μm carboxylate-functionalized polystyrene particles (PolyBead, USA) added as tracers. Solutions were placed into cylindrical hybridization chambers with a diameter of 13 mm and a height of 2 mm. The chambers sandwiched between a glass slide and a microscope cover slip. Light was introduced into the system via an HBO 100 mercury arc lamp equipped with a UV filter (Chroma inc.), which lowered the measured light intensity to roughly 32 mW/cm^2 as measured at 320 nm. This correlated to an intensity of 785 mW/cm^2 for the 2 mm spot with a wavelength range from 300-400 nm. Particles were observed using a Zeiss Axiovert 200 MAT microscope equipped with a Point Grey Flea2 camera. Pumping velocities were measured by monitoring the tracer particles using Tracker (Open Source Physics). Data was exported into Microsoft Excel and particle velocities calculated using root mean square analysis.

3.3.2 The Flat Surface Migration Rates

The flat surface trial was performed in a steel walled chamber (1 cm diameter) capped with glass cover slips on both ends. 5 nm AgNPs (Nanocs, 0.0011% w/w) were used with 0.0036% (w/w) each of 3, 10, and 20 μm tracer particles (PolyBead). These AgNPs were used in this trial since they demonstrated the highest ratio of convective flow rate to added material.

3.3.3 Convective Separation on an Incline

To study particle separation on an incline, square glass tubing (VitroCom, USA) with a length of 9 mm and a 3 by 3 mm cross section was sealed on one end using UV curing glue (RapidFix, USA) and the angles were varied using a hinge. A solution of citrate-stabilized AuNPs (0.07394 % w/w) was prepared using the seeded growth method outlined by Bast et al.,[28] and the size was determined to be 29±3 nm by dynamic light scattering. An aqueous solution was prepared containing a final concentration of 0.055 % (w/w) of the as-synthesized AuNPs, and roughly 0.005% (w/w) each of 3 μm and 10 μm carboxylate functionalized polystyrene microspheres. 500 μL of the prepared solution was used for each experiment.

3.4 Conclusions

In summary, the effect on convective pumping has been studied for gold and silver nanoparticles when irradiated with UV light in the 300-400 nm range. For citrate-stabilized gold, a maximum pumping rate is observed for particles of 80 nm which may indicate an optimized balance of absorption cross section and conversion efficiency of particles at this size. Silver exhibited the highest rate for 5 nm particles for which the SPR wavelength dips into the window of irradiation wavelengths. We also showed the effect that SPR wavelength has on heat generation and, in turn, pumping velocity by comparing silver particles of varying size. Particles closer to their SPR wavelength induced higher pumping velocities likely due to higher absorption and conversion of light at SPR wavelength. We determined that irradiating the particles at SPR wavelength overrides the size effects we observed previously.

In addition, we designed a system that can be used to separate particles of varying size using a UV light source and plasmonic nanoparticles. When adding light-responsive solutions to an inclined chamber, the competition between convective fluid pumping and gravitational forces create two separate groupings of particles. Larger particles do not collect as far up the chamber due to their higher settling rates while smaller particles are carried further up the chamber to collect. Continuous convective flows in the system hold the groups of particles in place and, when the light is turned off, the particles slowly fall down the incline. This system is a cost-effective and non-hazardous way to separate particles and could be used for both biological and inorganic applications. Overall, this we have provided a simple and controllable way for separating particles of various sizes and have explored the unique principles that govern self-assembly by convective pumping.

3.5 Acknowledgements

This work was made possible by NSF-CCI Award Number 1740630. Any opinions, findings, and conclusions or recommendations expressed in this chapter are those of the author and do not necessarily reflect the views of the National Science Foundation.

3.6 References

[1] S. Sengupta, D. Patra, I. Ortiz-Rivera, A. Agrawal, S. Shklyaev, K. K. Dey, U. Córdova-Figueroa, T. E. Mallouk, A. Sen, *Nat. Chem.* **2014**, *6*, 415–422.

[2] I. Ortiz-Rivera, T. M. Courtney, A. Sen, *Adv. Funct. Mater.* **2016**, *26*, 2135–2142.

[3] C. Zhou, H. Zhang, Z. Li, W. Wang, *Lab Chip* **2016**, *16*, 1797–1811.

[4] T. R. Kline, W. F. Paxton, Y. Wang, D. Velegol, T. E. Mallouk, A. Sen, *J. Am. Chem. Soc.* **2005**, *127*, 17150–17151.

[5] I. Ortiz-Rivera, H. Shum, A. Agrawal, A. Sen, A. C. Balazs, *Proc. Natl. Acad. Sci.* **2016**, *113*, 2585–2590.

[6] B. J. Zhang, Y. Li, X. Zhang, B. Yang, *Adv. Mater.* **2010**, *22*, 4249–4269.

[7] J. J. Mcdermott, A. Kar, M. Daher, S. Klara, G. Wang, A. Sen, D. Velegol, *Langmuir* **2012**, *28*, 15491-15497.

[8] F. Wong, A. Sen, *ACS Nano* **2016**, *10*, 7172-7179

[9] R. Niu, T. Palberg, *Soft Matter* **2018**, *14*, 3435–3442.

[10] B. M. Tansi, M. L. Peris, O. E. Shklyaev, A. C. Balazs, A. Sen, *Angew. Chem. Int. Ed.* **2019**, *58*, 2295–2299.

[11] A. O. Govorov, H. H. Richardson, *Rev. Lit. Arts Am.* **2007**, *2*, 30–38.

[12] M. T. Carlson, A. J. Green, H. H. Richardson, *Nano Lett.* **2012**, *12*, 1534–1537.

[13] X. Huang, M. A. El-Sayed, *J. Adv. Res.* **2010**, *1*, 13–28.

[14] M. L. Brongersma, N. J. Halas, P. Nordlander, *Nat. Nanotechnol.* **2015**, *10*, 25–34.

[15] R. J. Fortenbaugh, B. J. Lear, *Nanoscale* **2017**, *9*, 8555–8559.

[16] R. J. G. Johnson, J. D. Schultz, B. J. Lear, *Molecules* **2018**, *23*, 1234-1245

[17] M. T. Carlson, T. S. Barton, P. J. Tandler, H. H. Richardson, A. Govorov, *Mater. Res. Soc. Symp. Proc.* **2009**, *1172*

[18] O. M. Wilson, M. R. Knecht, J. C. Garcia-martinez, R. M. Crooks, *J.Am. Chem. Soc.* **2006**, *128*, 4510–4511.

[19] R. Fenger, E. Fertitta, H. Kirmse, A. F. Thunemann, K. Rademann, *Phys. Chem. Chem. Phys.* **2012**, *14*, 9343–9349.

[20] S. Sarina, E. R. Waclawik, H. Zhu, *Green Chem.* **2013**, *15*, 1814–1833.

[21] G. Von Maltzahn, J. Park, A. Agrawal, N. K. Bandaru, S. K. Das, M. J. Sailor, S. N. Bhatia,

Cancer Res. **2009**, *69*, 3892–3901.

[22] D. P. O. Neal, L. R. Hirsch, N. J. Halas, J. D. Payne, J. L. West, *Cancer Lett.* **2004**, *209*, 171–176.

[23] X. Huang, P. K. Jain, I. H. El-sayed, *Lasers Med. Sci.* **2008**, *23*, 217–228.

[24] Z. Qin, Y. Wang, J. Randrianalisoa, V. Raeesi, W. C. W. Chan, W. Lipinski, J. C. Bischof, *Sci. Rep.* **2016**, *6*, 1–13.

[25] M. Kim, J. Lee, J. Nam, *Adv. Sci.* **2019**, *6*, 1900471.

[26] R. K. Manna, O. E. Shklyaev, J. Kau, B. Tansi, A. Sen, A. C. Balazs, *ACS Appl. Mater. Interfaces* **2019**, *11*, 18004-18012.

[27] D. Velegol, in *Colloid. Syst.*, **2016**, pp. 95–111.

[28] N. G. Bast, J. Comenge, V. Puntes, *Langmuir* **2011**, *27*, 11098–11105.

Chapter 4

Direction-Controlled Micropumping with Multiple Flow Domains

The work in this chapter is a modified version of a manuscript in preparation adapted from Tansi, B.T.; Manna, R.K.; Shklyaev, O.L.; Peris, M.L.; Balazs, A.; Sen, A. Direction-Controlled Micropumping with Multiple Flow Domains. In Preparation

Up to this point, we have realized some strategies to promote fluid pumping, assemble colloidal crystals, and separate particles. This chapter will explore other ways to control fluid motion using light. Using specific photochemistry, both the rate and the direction can be affected, which allows for a unique approach for diagnostic tools as well as a means to control two flow domains independently of one another.

4.1 Introduction

Fluid micropumps offer a unique strategy by which to build a new class of diagnostic tools. Such systems are defined by their ability to induce localized and directed fluid motion on small scales and can be controlled by a suite of different parameters.[1] Many examples are based on small patches with specific reactivities, especially by catalysis, such as enzyme micropumps[2–6] and many inorganic pumps.[7–9] Pumps can be powered by many mechanisms, including electroosmosis,[8,10] diffusioosmosis,[11] and even bubble formation.[12] In these systems, the rate of fluid pumping is directly dependent on the concentration of a chemical fuel. Using this example, the simplest analyte would be the fuel itself. More broadly, any factor that will accelerate or inhibit pumping can be tested for. In the case of enzymes, any inhibitor will decrease the reaction

rate, providing a commensurate drop in pumping rate.[3] By back-calculating, we can again get a precise measure of the analyte concentration. To improve cost-efficiency and ease of use, recent reports outline a strategy to generate fluid pumping using colloidal nanoparticles rather than a fabricated patch.[13,14] To build on this principle, this report outlines a method to direct fluid pumping based on the presence of specific functional groups within solution. Rather than relying on the rate alone, the direction of fluid pumping can be changed entirely by using localized organic photochemistry, a clear indication of analyte. Additionally, we explore the presence of multiple flow domains based on near-surface gradients.

4.2 Results and Discussion

4.2.1 Downward Pumping Behavior

On the condition that hydrogen peroxide (H_2O_2) and a primary alcohol are present in an aqueous solution, downward pumping will occur under irradiation by ultraviolet (UV) light. This pumping is convective in nature, resembling the upward pumping described in the previous chapters, save for the direction. Our experiments suggest that this pumping is due to solutal buoyancy effects. This principle has been demonstrated for enzyme-based micropumps[3] and inorganic pumps using iodine.[15]

As a model system, a solution of ethanol (0.217M) and hydrogen peroxide (0.49M) was irradiated with a beam of UV light within a hybridization chamber (h=2mm, d=13mm) and convective flows developed around the incident area. As seen in Figure **4-1** (Supporting Video 4-1), the pumping velocity briefly increased before changing direction over the course of about 90 seconds of sustained irradiation.

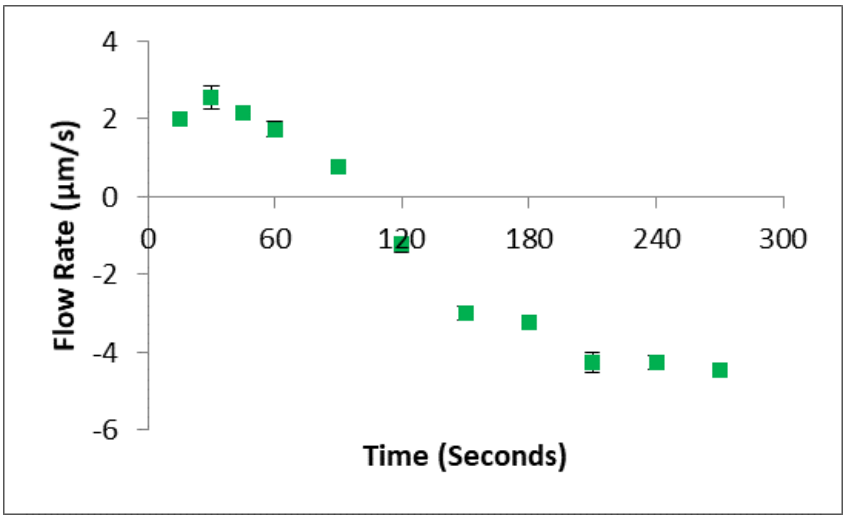

Figure **4-1**: The flow rate over time for a solution of ethanol (0.217 M) and hydrogen peroxide (0.49 M) under UV irradiation. The light is turned on at 30 seconds and the pumping direction changes shortly before the 120 second mark. These points represent the observed particle velocities at one quarter of the total chamber height and about 700 µm from the flow center. This can be clearly seen in Supporting Video 4-1.

A list of analytes tested for is given in Table 4-1. As noted, all of the primary alcohols considered will induce this downward pumping under the conditions tested, while other analytes will direct pumping upwards, including secondary alcohols, aldehydes, and pure hydrogen peroxide. Of these, hydrogen peroxide was seen to exhibit the fastest upwards pumping, however, the lower values for many of these can be attributed to higher viscosity owing to the added analyte compound. Generally, we see that the phenomenon of downward pumping occurs in the presence of primary alcohols with hydrogen peroxide and UV-irradiation. Isopropanol was used as a model secondary alcohol. Under UV irradiation, upward pumping was observed, however its isomer 1-propanol pumped downwards. The fastest downward pumping was generated by glycerol, for which we note the presence of two primary alcohol moieties per molecule. The only non-alcohol that promoted downward pumping was sodium formate, which is discussed in Appendix B.

Table **4-1**: The observed pumping rates and densities of a suite of tested compounds. Negative values indicate downward pumping. The concentration of each of these compounds was set at 0.217 M with an additional 0.49 M of H_2O_2. The rates were monitored by observing the outward motion of 10 µm carboxylate functionalized microparticles at 500 µm (one quarter of the total height) above the bottom surface. Each particle was tracked within 700-800 µm distance from the observed flow center under UV irradiation. *The downward pumping for 1-propanol was evident, but the rate was too low to get a reliable number given extraneous bulk flows.

Compound	**Rate (µm/s)**	**Density (g/ml)**
Glycerol	-6.4±0.6	1.26
Methanol	-4.5±0.3	0.792
Formaldehyde	7.0±0.6	0.815
Formic acid (pH 2)	5.4±0.4	1.22
Ethanol	-4.3±0.3	0.789
Acetaldehyde	5.7±0.4	0.788
Acetic Acid	4.6±0.5	1.05
1-propanol	-*	0.803
Propionaldehyde	1.40±0.07	0.810
Isopropanol	4.9±0.4	0.786
H_2O_2 (no additive)	7.2±0.6	1.45

4.2.2 Product Determination

Using nuclear magnetic resonance spectroscopy (NMR), three major products could be determined in the ethanol (0.217 M) and H_2O_2 (0.49 M) trials. These were acetic acid, acetaldehyde, and paraldehyde, the cyclic trimer of acetaldehyde.

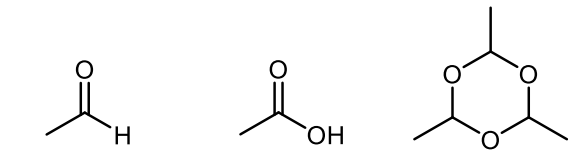

Acetaldehyde Acetic Acid Paraldehyde

Figure **4-2**: The reaction products from the ultraviolet irradiation of a solution containing EtOH and H_2O_2.

Using sodium trimethylsilylpropanesulfonate (DSS) as a reference standard, the concentrations could be monitored over time using ^{1}H-NMR , the results of which are given in Figure **4-3**. No products were observed without UV irradiation.

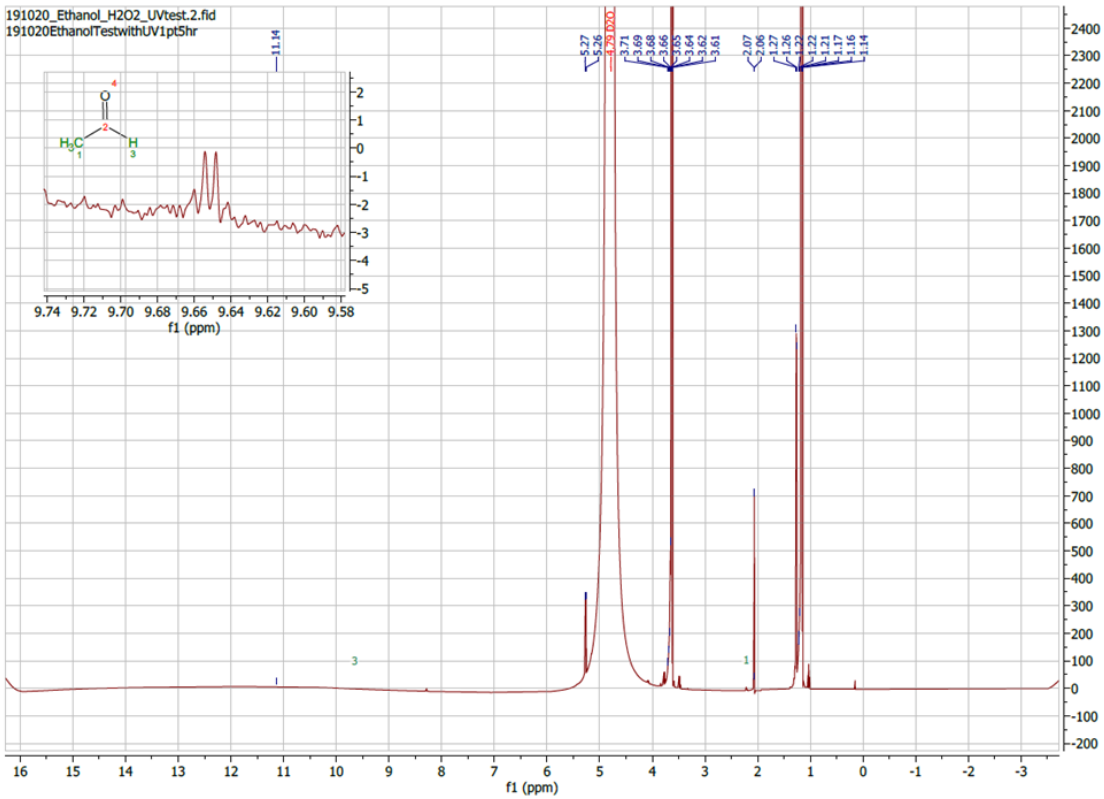

Figure **4-3**: ^{1}H-NMR spectra of ethanol and hydrogen peroxide after 90 minutes of UV irradiation. The remaining ethanol is seen by a quadruplet at 3.6 ppm and a triplet at 1.14 ppm. Acetic acid is seen as a doublet at 2.06 ppm and its presence is corroborated by the pH data in Figure **4-5.** Acetaldehyde appears as a quadruplet at 9.65 ppm (insert) and a small doublet at 2.1 ppm. The prominent peak at 4.79 is water.

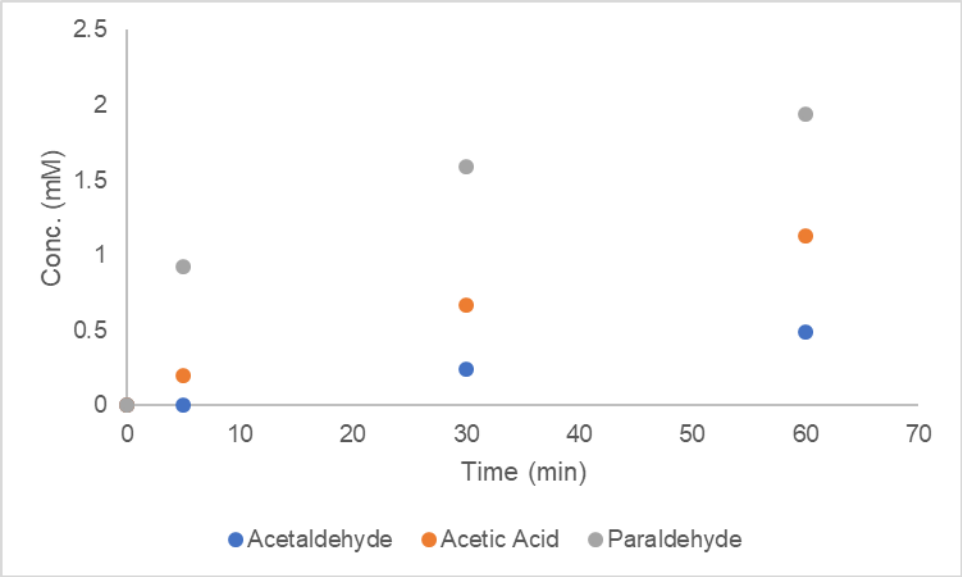

Figure **4-4**: The concentration of acetaldehyde (blue), acetic acid (orange) and paraldehyde (grey) during irradiation of an ethanol (0.217 M) and H2O2 (0.49 M) solution. The major product was paraldehyde, the cyclic trimer of acetaldehyde.

As mentioned, no products were detected without UV irradiation. On account of this result, it is likely that the reaction proceeds by the well-known homolysis of hydrogen peroxide.[16] Briefly, the O-O bond will cleave to yield two hydroxyl radicals, some of the most potent known oxidizing agents. These will rapidly attack most aliphatic compounds, including alcohols, with rate constants on the order of 10^9 $M^{-1}s^{-1}$.[17] The resultant oxidation is further corroborated by an observed decrease in pH over time, which can be attributed to the formation of acetic acid. The reaction between hydroxyl radicals and ethanol is well documented and known to promote the formation of acetic acid.[18]

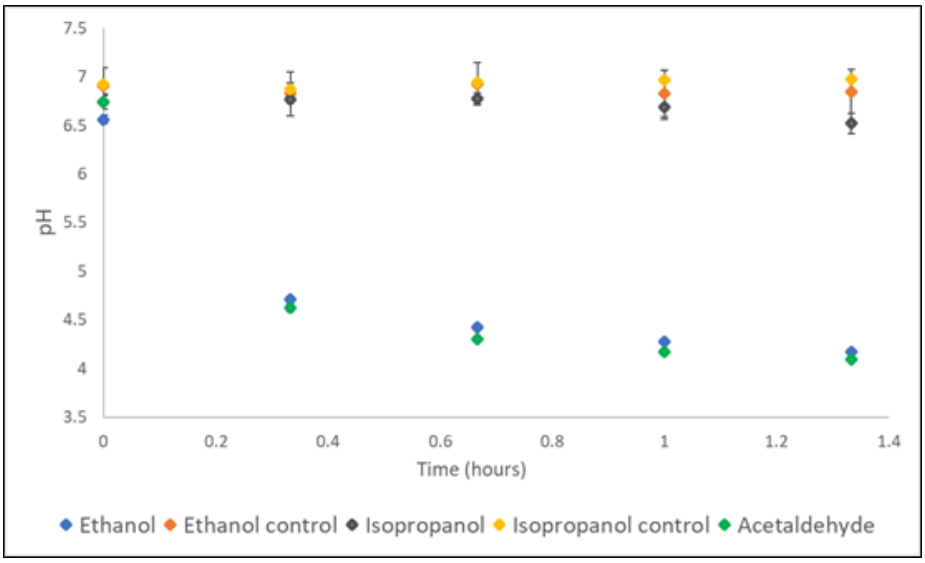

Figure 4-5: The pH drop over time for 0.217 M ethanol, and acetaldehyde, and isopropanol with 0.49 M H2O2. Under irradiation, ethanol and acetaldehyde exhibited comparable, precipitous drops in pH, while isopropanol maintained about the same pH throughout the observation time. The control samples were wrapped in foil and not irradiated.

4.2.3 Solutal Buoyancy Effects

Downward pumping has been demonstrated using enzyme micropumps.[2] In this study, the authors were able to develop a general rule to predict this behavior. When the ratio of diffusivities of the products and reactants, $\delta = D_P/D_S$, is greater than both 1 and the ratio of expansion coefficients, $\beta = \beta_P/\beta_S$, the pumping direction will become downwards with time. In their example, this was accomplished by the breakdown of urea into ammonium carbonate. However, the authors postulated that reversal can also occur if the ratio of diffusivities is below 1 and smaller than the ratio of expansion coefficients (i.e. if $\delta < 1$ *and* $\delta < \beta$). With acetaldehyde, paraldehyde, and acetic acid as the major products, the latter case applies to this system. As of this writing, preliminary simulation results show qualitative agreement with our experimental results and will be included in the finished manuscript.

Table **4-2**: The density, diffusivity, molar mass, and solutal expansion coefficients of relevant species in the reaction involving ethanol and hydrogen peroxide under UV irradiation.

	Density ρ (g/cc)	Diffusivity D (m^2/s)	Molar mass m_m (g/mol)	Expansion coefficient β (M^{-1})
Water	1.00	-	18.015	-
Hydrogen Peroxide	1.45	$1.43 \cdot 10^{-9}$	34.015	0.01056
Ethanol	0.7893	$1.21 \cdot 10^{-9}$	46.069	-0.01229
Acetic Acid	1.049	$0.989 \cdot 10^{-9}$	60.052	0.00280
Acetaldehyde	0.784	$1.23 \cdot 10^{-9}$	44.053	-0.01213
Paraldehyde	0.996	$0.75 \cdot 10^{-9}$	132.16	-0.00053

Provided that the reaction from ethanol to acetaledehyde exhibits a sufficiently higher reaction rate that the reaction of acetaldehyde to acetic acid, the rule holds for both the ratio of diffusivities and expansivities. The reaction to yield paraldehyde may inhibit the second step enough for the correct conditions to be met. Since the diffusivities are lower for the products, a propagating low-density wave front will move away from the irradiated region. This allows for many crazy things to happen. Since hydrogen peroxide is consumed more quickly (also reacts with acetaldehyde) than ethanol, this change will eventually happen, at which point the values are aligned with the second case considered in Ref. 2. More succinctly, the conditions are met as the values evolve with time. Just as we see in the experiments, downward pumping is not observed immediately. If the concentrations given in Figure **4-4** seem low, consider that the change only needs to occur within the irradiated area and that the concentration measurements are of the bulk solution.

4.2.4 Pumping by Infrared Irradiation

The effect of wavelength was also determined by irradiating the solution with an infrared laser (780nm). An identical sample of glycerol and H_2O_2 sample was prepared as that tested in Table **4-1**. Whereas UV light directed pumping downward, infrared radiation was seen to direct pumping upwards at a rate of 18±3 μm/s. This was expected due to the strong absorption of infrared light by water. Whether or not reactions are taking place, the solutal buoyancy effects will be generously overwhelmed by the amount of heat being produced locally. Although the light-source used in this experiment was considerably different in terms of spot size and intensity, this serves as a demonstration of how rate and direction can both be controlled by the light source.

4.2.5 Near Surface Effects

While the bulk solution is directed according to solutal buoyancy effects, another interesting behavior is observed along the bottom surface of the cell. Upon settling, carboxylate-functionalized polystyrene particles of 3 μm and 10 μm will migrate towards the irradiation center despite the convective flow working against it (Figure **4-6**). As seen in Supporting Video 4-2, particles will change direction immediately upon reaching the bottom of the cell. Since ionic species are being produced in the form of small organic acids, this motion is likely due to diffusioosmosis.

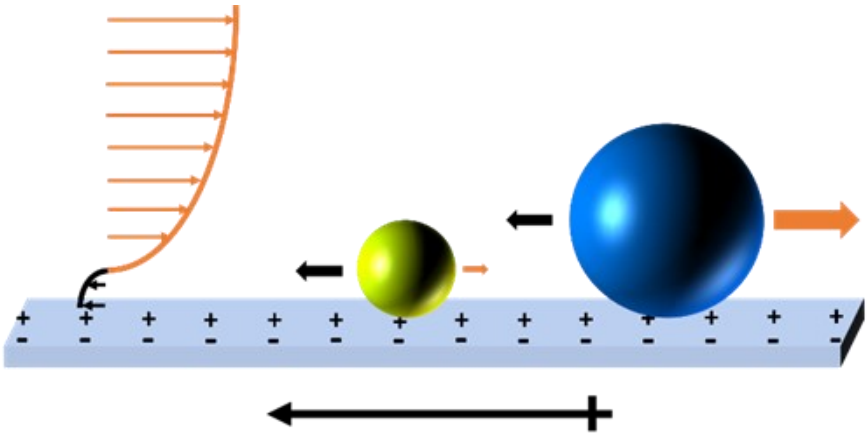

Figure 4-6: The migration direction on the surface demonstrates a dependence on particle size. The drag force due to the bulk fluid pumping is represented by the orange arrows and the effect of diffusioosmosis is represented in black. Larger particles will feel more of the convective roll by simply extending further into the solution above the surface.

Given a negatively charged surface and an electric field directed inward (i.e. higher diffusivity of the cation than anion) fluid flow near the surface will arise and be directed inward owing to the positively charged double layer. By generating weak acids where the cation is a proton, this result can be expected. Since the bulk fluid pumping is convective, the rate near the surface reduces to zero and other effects can easily dominate for particles that are sufficiently close. To confirm this hypothesis, the sign of the surface zeta potential was changed by adding the cationic surfactant cetyltrimethylammonium bromide (CTAB) at a concentration of 0.1 mM. Particles were then seen to migrate outwards in the direction of the convective flows. The possibility of diffusiophoresis can be eliminated by considering the direction of the gradient and the negative surface charge of the particles. They would be expected to move outward.

Because the gradient effect dominates near to the surface, the primary convective flows can still direct the motion of sufficiently large particles. Figure **4-7** and Supporting Video 4-3 display this principle for the case of acetaldehyde while exhibiting upward pumping in the presence of H_2O_2 and 0.1mM CTAB. Although acetaldehyde would direct pumping upwards, it still

produced acetic acid and could therefore produce this near-surface effect. Here, smaller particles (10 µm) move outward due to diffusioosmosis near the positively charged surface while larger particles (20 µm) move inward. Some examples of particle separation exist based on a balance of forces such as fluid drag and gravity,[14] but this is a rare instance of different directionalities based on competing flow regimes. In this way, the direction of transport in the bulk and near surfaces can be carefully tailored independently of one another.

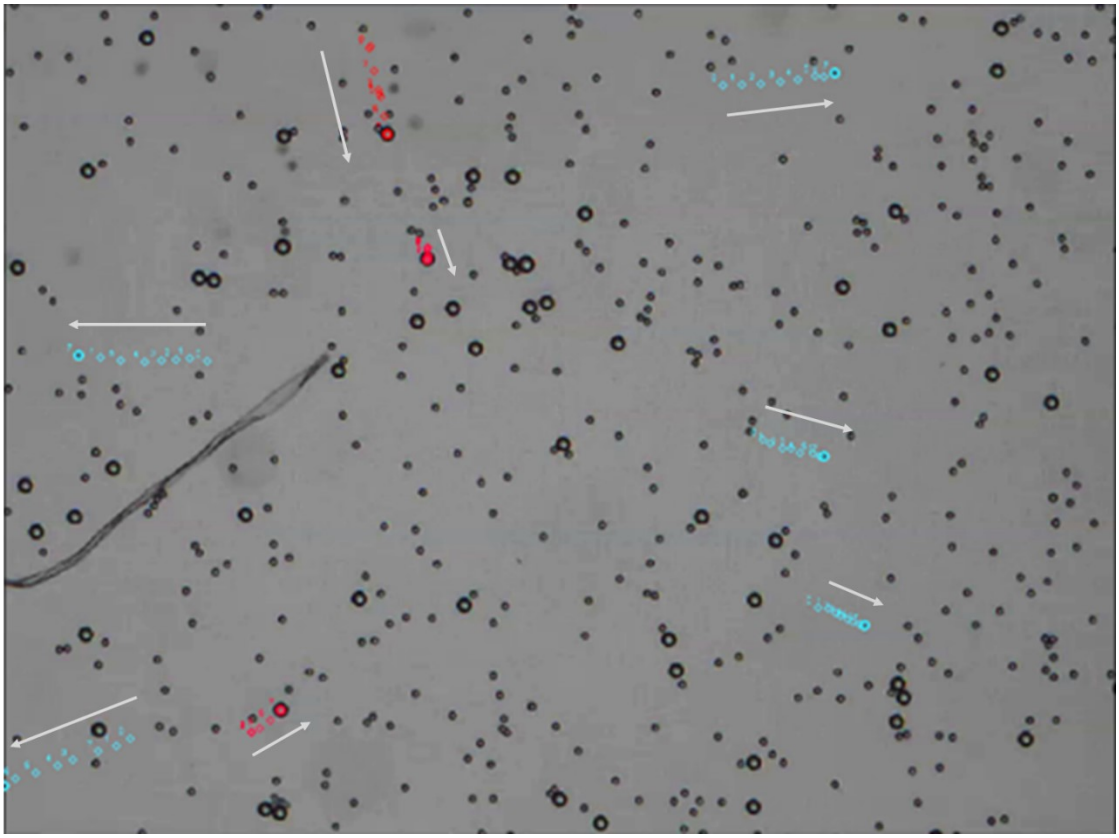

Figure 4-7: The surface migration of 10µm and 20µm tracer particles during the upward pumping of acetaldehyde/H2O2 solution under irradiation. The red tails represent the motion of 20µm particles as they move inwards towards the irradiation center. Blue tails are of the 10µm tracer particles moving outward, responding to near surface gradients. Due to the high concentration of CTAB, there is significant sticking at a short timescale near the surface. The arrows are to help indicate the direction of migration. The bottom of the frame is 1528 µm across.

4.2.6 Exclusion Rings

One of the surprising results of these directed bulk flows and near surface flows is the ability to create exclusion rings. In the case of outward pumping, this can be accomplished by the directed settling of particles as seen in Figure **4-8**. Here, a white ring is seen inside of the hybridization chamber with a largely empty volume in the middle.

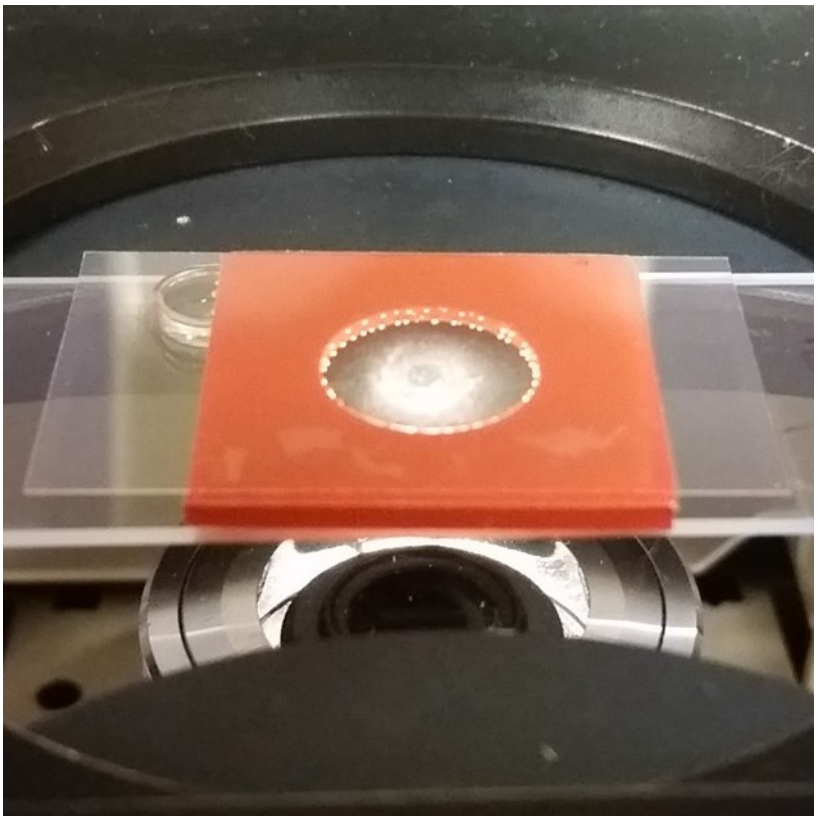

Figure 4-**8**: An exclusion ring forms within the chamber due to directed settling after an hour of downward convection. Here, the powdery, white ring of 3 µm and 10 µm microparticles is visible near the center of the cell. Away from the surface, and in the bottom half of the chamber, the convective flows are directed away from the irradiation center, leading to the pattern shown here. The set-up shown here is the same one used for all velocity measurements as well as observing the near-surface behavior. The height is 2 mm and the diameter is 13 mm. Some bubbles form over time and are visible around the edge of the cell. These are attributed to the thermal breakdown of hydrogen peroxide as a side reaction. Glycerol was used as the alcohol in this trial.

Alternatively, an exclusion ring may form if the diffusioosmotic flows are directed outwards. By adding 0.1 mM CTAB to a trial with acetaldehyde (0.217 M) and H_2O_2 (0.49 M), an exclusion ring will eventually develop despite the bulk pumping carrying particles inwards in the lower half of the chamber. Using the particle counting feature from imageJ (NIH), the profile in Figure **4-9** was measured for an exclusion ring over the course of about 20 minutes.

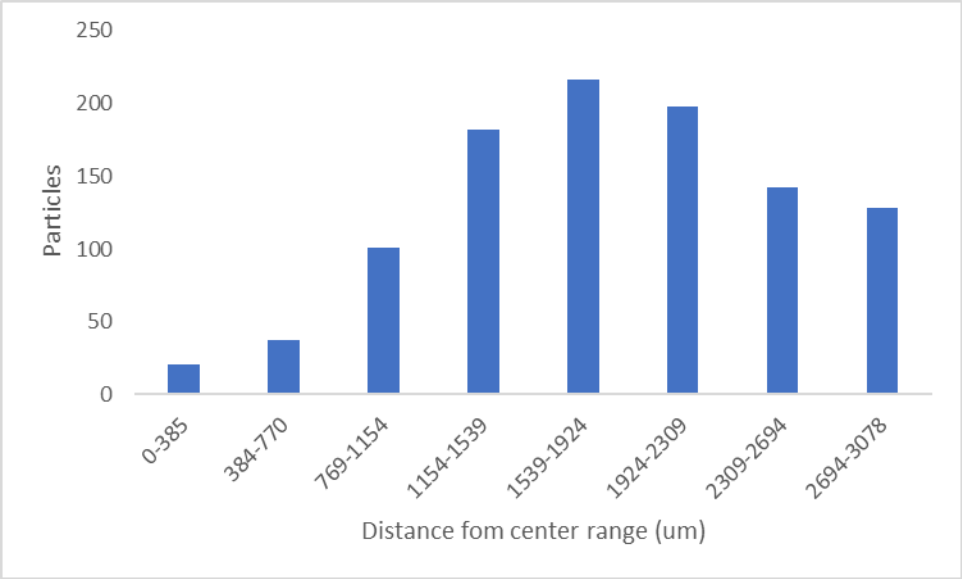

Figure 4-9: The particle distribution moving radially outward along the bottom surface in the acetaldehyde/H2O2 system with CTAB. The leftmost points correspond to the center of the hybridization chamber. Despite convective flows moving inward in this case, the near-surface flows dominated for settled particles of 3 and 10 µm diameters. The number of particles is taken from a series of images with dimensions of 384.8 x 287.1 µm using a 20x objective. ImageJ was used to count the number of particles within each frame. These images were taken after 20 minutes of irradiation and formed an exclusion ring comparable to that from directed settling as in Figure **4-8**

4.3 Experimental

4.3.1 Alcohol and Peroxide Experiments

Samples were prepared with 0.217 M of the alcohol and 0.49 M hydrogen peroxide in water. Unless noted otherwise, 3 μm polystyrene carboxylate particles were added for observation of the flows. The UV lamp directed light through a 5x objective, which loosely collimated the light into a 2mm diameter beam with an intensity of 780 mM/cm2. Upon irradiation, the solution would begin to exhibit pumping in a direction dependent on the analyte tested. For conditions under which upwards pumping was observed, this motion began almost immediately. For downwards pumping (i.e. primary alcohols), there was a delay of about 2 minutes before pumping was observed. All trials were performed in a 2mm thick hybridization chamber with a 13 mm diameter. Bulk pumping observations were made at 500 μm above the surface (i.e. one quarter cell height) and the rates were measured using particles that were about 700μm away from the flow center. This was done for consistency as the distance from the center affected the observed in-plane velocities. Tracker (Open Source Physics) was used for all measurements

4.3.2 Near-Surface Trials

To probe the behavior near the bottom surface of the cell, several sizes of microparticles were used. For the trials with CTAB, the zeta potentials of the glass surface was approximated by measuring that of 1 μm silica nanoparticles (US Nanomaterials) using a ZetaSizer Nano (Malvern Instruments). The values were seen to change from -35±4.15 for the unfunctionalized beads to 43±5 with added CTAB (0.1 mM). The surface charge of the carboxylate functionalized polystyrene particles changed from -32±1 and 38.8±0.4 mV. We emphasize that the migration direction fits the diffusioosmosis hypothesis.

4.3.3 Infrared Irradiation Trials

The effect of infrared irradiation was explored by using a 780 nm laser with an intensity of 235 mW. The motion of particles was observed in the same chamber and conditions used for the ultraviolet trials. The laser spot was less than 10μm in diameter, and the beam was not collimated, meaning that most of the heat was generated at a point and not within a column such as in the UV experiments.

4.3.4 pH Trials

A 900 uL solution was prepared with 0.217M of the chosen alcohol and 0.49M Hydrogen peroxide. The sample was added to a glass vial, which was irradiated on the microscope with a 780mW/cm^2 intensity in a 2mm spot size that was roughly collimated. Once every twenty minutes, the sample was removed and tested with a micropH probe in triplicate measurements using an Orion™ PerpHecT™ Ross™ Combination pH microelectrode (Thermo Scientific).

4.3.5 NMR Experiments

Products were determined by nuclear magnetic resonance (NMR). The peak splitting and relative concentrations proved the existence of acetaldehyde, paraldehyde, and acetic acid. A 900 uL solution was prepared with 0.217M of the chosen alcohol and 0.49M Hydrogen peroxide in deuterium oxide (D_2O). The sample was added to a glass vial, which was irradiated on the microscope with a 780mW/cm^2 intensity in a 2mm spot size that was roughly collimated. For product determination, this sample was added to an NMR tube after about 90 minutes of irradiation.

To monitor the rate of product formation and the relative concentrations, a 60 µL aliquot was removed at 0, 5, 30, and 60 minutes and was added to 540 µL of D_2O with a known concentration of sodium trimethylsilylpropanesulfonate (DSS) as a standard. The result of this trial with EtOH and H_2O_2 is given in Figure **4-4**.

4.4 Conclusions

We have demonstrated a method of light-based direction-controlled fluid pumping based on the presence of certain analytes. The direction of fluid pumping and surface migration direction can be tuned independently of one another based on surface charge and on the analyte chosen for observation. The convective pumping method outlined above will reliably indicate the presence of primary alcohols in a solution that does not meaningfully absorb between 300-400 nm save for hydrogen peroxide. To the authors knowledge, the size-based migration along the surface is the only example of selection using the competition between chemiphoresis and fluid drag due to convective pumping. This unique capability holds promising potential in sensing and microscale assembly applications.

4.5 Acknowledgements

This work was made possible by NSF-CCI Award Number 1740630. Any opinions, findings, and conclusions or recommendations expressed in this chapter are those of the author and do not necessarily reflect the views of the National Science Foundation.

4.6 References

[1] C. Zhou, H. Zhang, Z. Li, W. Wang, *Lab Chip* **2016**, *16*, 1797–1811.

[2] I. Ortiz-Rivera, H. Shum, A. Agrawal, A. Sen, A. C. Balazs, *Proc. Natl. Acad. Sci.* **2016**, *113*, 2585–2590.

[3] I. Ortiz-Rivera, T. M. Courtney, A. Sen, *Adv. Funct. Mater.* **2016**, *26*, 2135–2142.

[4] S. Sengupta, D. Patra, I. Ortiz-Rivera, A. Agrawal, S. Shklyaev, K. K. Dey, U. Córdova-Figueroa, T. E. Mallouk, A. Sen, *Nat. Chem.* **2014**, *6*, 415–422.

[5] R. Munteanu, M. N. Popescu, S. Gáspár, *Condens. Matter* **2019**, *4*, 73–93.

[6] S. Maiti, O. E. Shklyaev, A. C. Balazs, A. Sen, *Langmuir*, **2019**, *35*, 3724-3732.

[7] F. Wong, K. K. Dey, A. Sen, *Annu. Rev. Mater. Res.* **2016**, *46*, 407-432

[8] T. R. Kline, W. F. Paxton, Y. Wang, D. Velegol, T. E. Mallouk, A. Sen, *J. Am. Chem. Soc.* **2005**, *127*, 17150–17151.

[9] V. Yadav, H. Zhang, R. Pavlick, A. Sen, *J. Am. Chem. Soc.* **2012**, *134*, 15688-15691.

[10] R. Niu, T. Palberg, *Soft Matter* **2018**, *14*, 3435–3442.

[11] J. J. Mcdermott, A. Kar, M. Daher, S. Klara, G. Wang, A. Sen, D. Velegol, *Langmuir* **2012**, *28*, 15491-15497.

[12] A. A. Solovev, S. Sanchez, Y. Mei, O. G. Schmidt, *Phys. Chem. Chem Phys.* **2011**, *13*, 10131–10135.

[13] B. M. Tansi, M. L. Peris, O. E. Shklyaev, A. C. Balazs, A. Sen, *Angew. Chem. Int. Ed.* **2019**, *58*, 2295–2299.

[14] R. K. Manna, O. E. Shklyaev, J. Kau, B. Tansi, A. Sen, A. C. Balazs, *ACS Appl. Mater. Interfaces* **2019**, *11*, 18004-18012.

[15] M. Li, Y. Su, H. Zhang, B. Dong, *Nano Res.* **2017**

[16] F. Cataldo, *New Front. Chem.* **2014**, *23*, 99–110.

[17] B. Ervens, S, Gligorovski, H. Herrmann, *Phys. Chem. Chem. Phys.* **2003**, *5*, 1811–1824.

[18] E. Bothe, M. N. Schuchmann, D. Schulte-Frohlinde, C. von Sonntag, *Z. Naturforsch. B* **1983**, *38*, 212–219.

Chapter 5

Future Work

Many possibilities are opened up by the use of light for fluid pumping. The previous chapters outline strategies by which to assemble colloidal crystals, separate particles by size, and to detect target analytes based on pumping direction. To build on this framework, there are several thrusts that warrant specific attention. This chapter will serve as a guide to future research on the topic.

5.1 Colloidal Crystal Self-Assembly

Colloidal crystals like that in Chapter 2 have been increasingly studied due their rich potential in many fields, especially those that rely on optoelectronic responses.[1] Among other ends, dielectric structures have been seen to yield structural color,[2] controlled porosity can contribute greatly to electrodes or capacitors,[3] and arrays of responsive particles can be used as actuators.[4] These can be assembled in a growing suite of methods,[5] but the use of fluid drag, as outlined in Chapter 2, offers a unique and powerful tool. As highlighted in Figure 2-7, fluid pumping has a tremendous medium independence. When designing colloidal crystals for any application, the use of heat in this manner could allow for assembly without an explicit attraction between the particles involved. The requirements for particle interactions can be in part or entirely removed if the crystals are assembled in this manner. Because of this, many existing applications can possibly be improved upon.

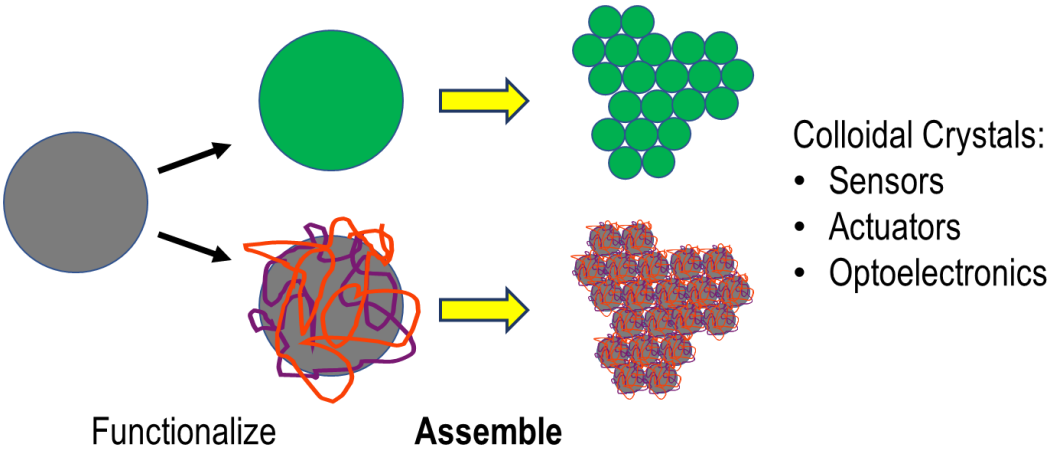

Figure 5-1: A generalized strategy for device assembly. The suite of colloidal crystal-based devices can be rapidly built up by performing assembly with relative disregard for how the particle is functionalized.

To support further investigations, it is necessary to address the tracer particle size dependence elucidated in Chapter 3. Recall that smaller particles *feel* less of the bulk fluid pumping and will migrate more slowly. One can reasonably expect that there is a limit at which the directed migration will no longer overcome diffusion. However, the settling velocity is also influenced by particle size, so meaningful collection may be a challenge when considering much smaller sizes. The settling rate of a particle can be predicted from Stokes Law as seen in Equation 3.1. To take an example, the settling rate for a 1 μm polystyrene particle (1060 kg/m^3) is about 18 nanometers per second. If we used the 2 mm chamber from Chapter 4, then it would take over 30 hours for all of the particles to settle out. As such, there is a practical limitation against anything that would be considered "nanoscale." Needless to say, the industrial usefulness is quickly mitigated for sufficiently small particles.

5.2 Fluorescence Quenching and Pumping

When a photon is absorbed by a plasmonic nanoparticle, an electron becomes excited. One of three things then need to happen with this newfound energy. Either light is given off in the form of fluorescence or perhaps phosphorescence, it can contribute to chemical reactions, or it gives off heat. Oftentimes, this will be a combination of effects and, more often than not, the heat is considered wasted energy. However, this wasted energy is the backbone of photothermal therapies[6–9] in addition to the sensing and assembly strategies discussed in earlier chapters. In order to encourage this heat generation, the other two mechanisms need to be mitigated. Indeed, there have been studies of increased photothermal conversion efficiency arising from fluorescence quenching.[10,11] This principle has been applied to biologically relevant conditions, but the use in fluid pumping has been overlooked to present.

The best class of particles for this investigation would likely be quantum dots (QDs). These particles will often exhibit near unity quantum yields, which is useful for many industrial applications. However, there are many species that will quench their fluorescence.[10] So long as the absorption isn't commensurately reduced, any of these additives could ostensibly be tested for. If there is a concentration dependence, then the fluid pumping rates will reveal not only the presence, but the concentration of analytes. A good comparison to the proposed system is that of enzyme inhibitor assays.[12] Briefly, the addition of an enzyme's inhibitors will decrease the pumping rate and the decrease can be used to measure below parts-per-billion concentrations of such toxins as mercury and cyanide. A diagnostic pump based on fluorescence quenching would operate the same way, except that the pumping rate will *increase* with added analyte.

The likely criticism of the above proposal is that a decrease in fluorescence would be easily observable and defeat the purpose of monitoring the pumping rate. However, the detection limit may be much lower using this method. Consider this. A fluorescence quantum yield of 95% still

generates too much heat for some applications,[13] and a local temperature change of 1 K will promote 100 μm/s fluid velocities.[14] Additionally, the highest observed pumping rates in the enzyme-inhibitor assay were 2.5 μm/s, which decreased by as little as 0.5 μm/s to reveal the presence of toxins. In short, it takes an incredibly small effect to yield dramatic fluid pumping velocities and it only requires 1/2000th of that effect to measure an analyte. Once the particle type, quenching agent, and light-source are defined, this system may be incredibly fruitful. Given time, it may become the industry standard for low limit analyte detection.

5.3 Photoacid Generators

Photoacid generators are a self-explanatory class of molecules. When irradiated with light of the proper wavelength, these compounds will break down to yield strong acid products. An investigation was performed to assess the ability of these products to rive fluid pumping.[15] Generally, these are water insoluble and therefore require a co-solvent. Without this co-solvent, the crystals will sink to the bottom of a cell and constitute a patch. In this past study, they were able to promote electroosmotic flows, however, this may not be the only strategy available to direct fluid pumping. Solutal buoyancy effects will also contribute to directed pumping as demonstrated by some preliminary work. This section will present the results of the experiments and outline the next steps in this investigation.

5.3.1 Experimental Results

To probe the effects of UV on homogeneous solutions of photoacid generators, 0.29mM N-hydroxynaphthalamide triflate (Figure **5-1**, Sigma-Aldrich) was prepared in water with N-methyl pyrrolidone as a co-solvent (14%). Sodium Nitrate (100 mM) was also added in order to quench ion gradient effects and yield better stability. Upon irradiation, the solution would pump upwards, which is attributed to the strong UV-absorption consistent with its aromatic structure. However, upon turning off the light, the solution would change direction and begin to pump downwards at rates similar to those observed for the alcohol and peroxide system (~7μm/s).

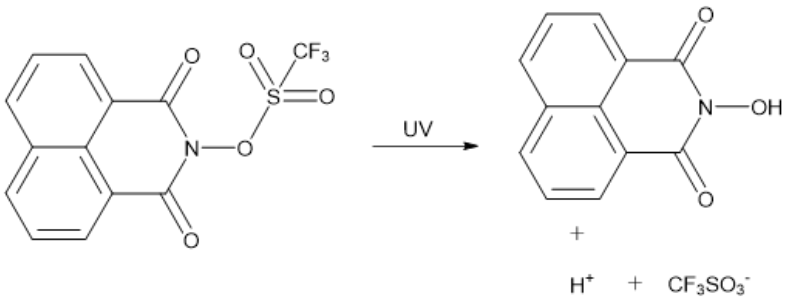

Figure **5-2**: The reaction of N-hydroxynaphthalimide triflate under UV irradiation to yield triflic acid. The aromatic structure is also present in the product, which helps to maintain UV absorption even after reaction has occurred.

We attribute the downwards pumping to the formation of triflic acid under UV-irradiation. The diffusivity of heat is greater than that of its dissociation products by more than an order of magnitude (1.3×10^{-7} m^2/s vs 9.31×10^{-9} m^2/s for a proton in water) [cite], allowing the cooled solution to retain a high local ionic strength and commensurately higher density. This downward pumping will stop after several minutes as the solution returns to an equilibrium state.

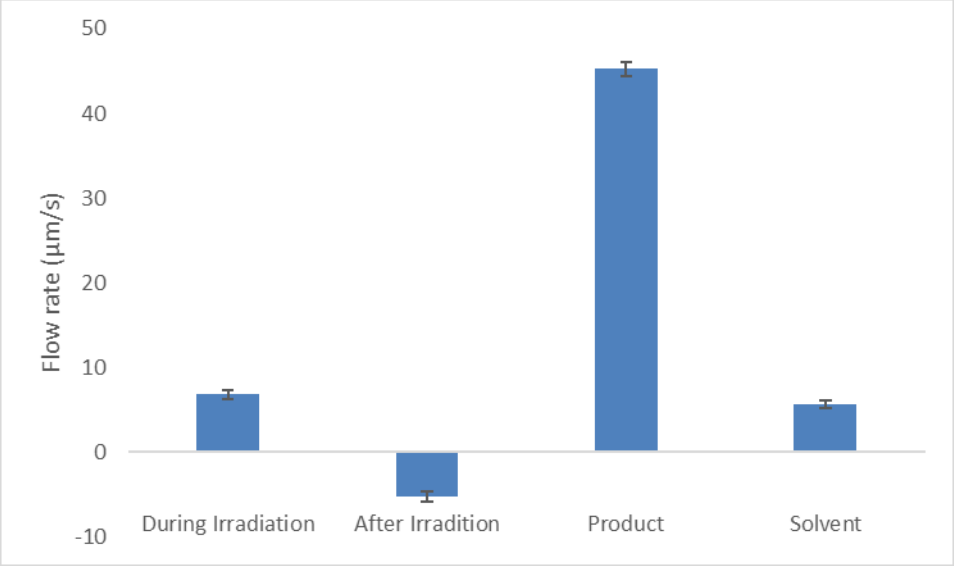

Figure 5-3: The flow rates of the PAG solution during and after UV irradiation compared to the reaction product and the solvent. No pumping was observed for water without the NMP co-solvent.

As seen in Figure 5-2, the product will exhibit rapid fluid pumping. This suggests one of two things. First, the absorbed light energy may be directed into the chemical change with great efficiency. Otherwise, the product formation significantly inhibits the upward pumping rate. Owing to the heat of reaction, the answer requires more robust experimental work to elucidate.

A drop in pH from about 8 to 6.5 was observed over 40 minutes of irradiation from a handheld UV lamp at 365 nm. A change was also observed in the UV-vis spectra for this sample. The peak intensity around 350 nm dropped precipitously during irradiation. For this study, 0.29mM N-hydroxynaphthalamide triflate (Figure 4, Sigma-Aldrich) was prepared in water with N-methyl pyrrolidone as a co-solvent (14%) and 100mM sodium nitrate to again quench ion gradient effects and yield better stability. Upon irradiation, the solution would pump upwards, which is attributed to the strong UV-absorption consistent with its aromatic structure. However, upon turning off the light, the solution would change direction and begin to pump downwards at rates of about 7 µm/s (Supporting Video 5-1).

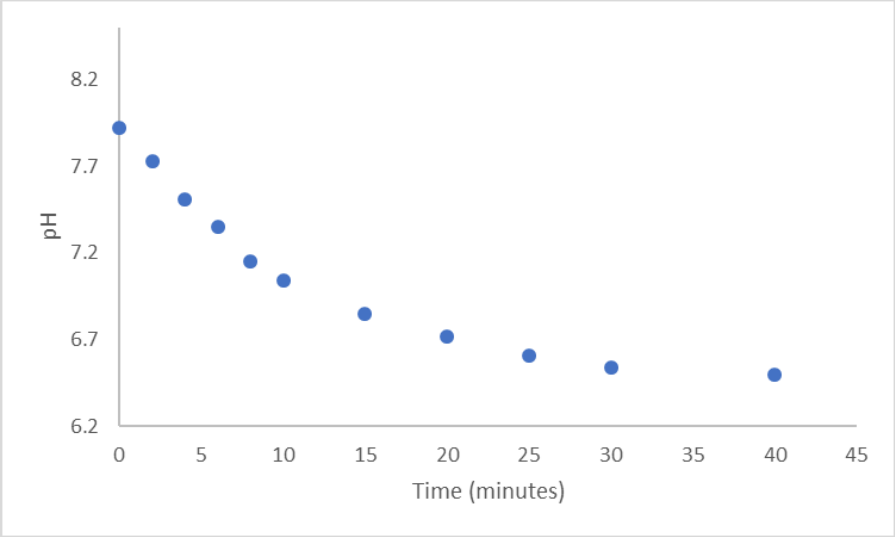

Figure 5-4: The pH of the PAG solution over time during irradiation with a handheld UV lamp. The decrease is a direct result of the rising concentration of triflic acid.

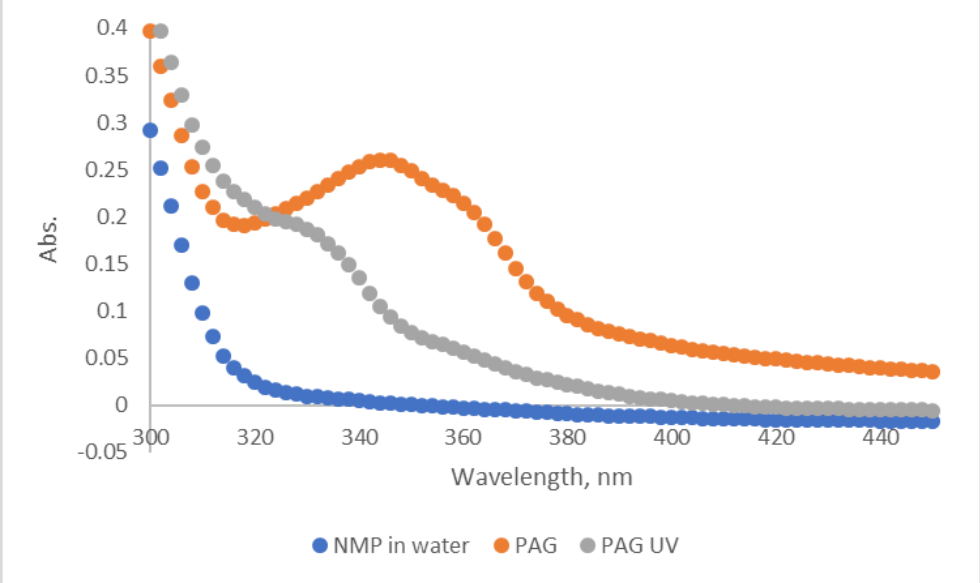

Figure 5-5: The UV absorption by the solvent solution and N-hydroxynaphthalimide triflate before and after irradiation. Irradiation of the photoacid generator caused a significant absorption decrease in the 300-400 nm range as the reaction occurred. This trial was performed using a handheld UV lamp of 365 nm wavelength. While this promoted the reaction, the intensity was substantially lower than in that used for the investigations in previous chapters.

5.3.2 The Next Steps

One of the interesting features from the reversible pumping system (Chapter 4) is that the downward flows would occur under sustained irradiation. It is likely that this same effect can be managed using photoacid generators like that described above. Work is needed to get the conditions correct in order for this to happen and it would be helpful to first identify a co-solvent that doesn't absorb UV light. As noted above, a 14% solution of NMP will exhibit upwards pumping before anything else is added. Removing this limitation may be enough by itself. Alternatively, there are other PAGS that absorb in the visible light region. This would work just as well, especially if a similar color change is observed upon doing so.

The other major item is that triflic acid is comprised of counterions with significantly different diffusivities. This means that diffusiophoresis and diffusioosmosis could factor heavily into the behavior of suspended particles. A small observation was that the addition of salt would stabilize the flows. Ostensibly, this is because the particles were no longer responding to ionic gradients in addition to the bulk flows. In any event, a similar dual-mechanism to that in Chapter 4 should be easily attainable. The ability to produce two flow domains is unusual and warrants deeper investigation because of its potential in surface patterning and in concentrating analytes.

5.4 Building the Catalog

The rule that we began with should direct the future of this research. Anything that meaningfully effects the rate of fluid pumping is something that can be tested for. While there are many potential applications for directed fluid pumping, none are as promising as diagnostic tools and perhaps water testing. The work in previous chapters offers a strategy by which to accomplish this. While the photothermal effect has been increasingly studied, its use in fluid pumping has been

limited to very few investigations. There are many particle types that will exhibit the photothermal effect and any of these can translate to directed fluid pumping. Many of these particles also offer unique photochemistry and have different factors influencing their plasmonic nature (Section 5-2). Looking forward, the catalog of particles should be built, and in doing so the number and types of analytes will continue to grow. In time, the gold standard will be biomarkers that are hard to identify by other means, allowing for early detection. During the preparation of this dissertation, most Americans are being told to stay home to prevent the spread of the COVID-19 pandemic. There is a lot of work to do, but perhaps we can slow down the next viral threat using a microscope, a UV lamp, and a little ingenuity.

5.5 References

[1] M. J. Solomon, *Langmuir* **2018**, *34*, 11205-11219

[2] A. G. Dumanli, T. Savin, *Chem. Soc. Rev.* **2016**, *45*, 6698-6724.

[3] H. Zhang, X. Yu, P. V Braun, *Nat. Nanotechnol.* **2011**, *6*, 277–281.

[4] T. Brunet, J. Leng, O. Mondain-Monval, *Science* **2013**, *343*, 323-324 .

[5] V. Lotito, T. Zambelli, *Adv. Colloid Interface Sci.* **2017**, *246*, 217–274.

[6] X. Huang, M. A. El-Sayed, *J. Adv. Res.* **2010**, *1*, 13–28.

[7] J. Estelrich, M. Ant, *Molecules* **2018**, *23*, 1567-1592.

[8] D. P. O'Neal, L. R. Hirsch, N. J. Halas, J. D. Payne, J. L. West, *Cancer Lett.* **2004**, *209*, 171–176.

[9] M. Kim, J. -H. Lee, J. -M. Nam, *Adv. Sci.* **2019**, *6*, 1-23.

[10] L. Zhao, Y. Liu, R. Xing, X. Yan, *Angew. Chem. Int.Ed.* **2019**, *59*, 3793–3801.

[11] W. Du, Y. Chong, X. Hu, Y. Wang, Y. Zhu, J. Chen, X. Li, Q. Zhang, G. Wang, J. Jiang,

G. Liang *Adv. Funct. Mater.* **2020**, *30*, 1–14.

[12] I. Ortiz-Rivera, T. M. Courtney, A. Sen, *Adv. Funct. Mater.* **2016**, *26*, 2135–2142.

[13] D. A. Hanifi, N. D. Bronstein, B. A. Koscher, Z. Nett, J. K. Swabeck, K. Takano, A. M. Schwartzberg, L. Maserati, K. Vandewal, Y. van de Burgt, A. Salleo, A. P. Alivisatos *Science* **2019**, *363*, 1199–1202.

[14] B. M. Tansi, M. L. Peris, O. E. Shklyaev, A. C. Balazs, A. Sen *Angew. Chem. Int. Ed.* **2019**, *58*, 2295–2299.

[15] V. Yadav, H. Zhang, R. Pavlick, A. Sen, *J. Am. Chem. Soc.* **2012**, *134*, 15688-15691.

Appendix A

Theoretical Complement to Chapter 2

To verify that the thermal buoyancy mechanism is responsible for the experimental observations, we developed a computational model for the corresponding system. As detailed in the Supporting Information, we consider a rectangular chamber (Supporting Figure 2-1) which contains an aqueous solution of uniformly dispersed gold particles with radius r_p =10.5 nm. Due to the particles' small radii, the sedimentation can be ignored and the particles are treated as a continuous field of a solute, with a uniform constant concentration C (particles m^{-3}), which is known from the experiment. When irradiated with UV light, the solution within the radius of the light beam, R_1=1 mm, begins to heat up. In particular, each gold particle in this region absorbs light and generates an amount of heat q=1.39 pW, calculated using the Mie theory for the case when r_p is much smaller than the wavelength of the light.[1] A solution with a concentration C of particles generates a maximum total amount of heat $Q=qC$ (Wm^{-3}). To describe the spatial distribution of the irradiated particles, we introduce a function f, which equals one when the particles are located within the region exposed to the light beam and zero otherwise. Then, the distribution of the heat sources in the solution is $Qf(r)$.

The dynamics of the non-uniformly heated fluid were modeled by solving the continuity, Navier–Stokes, and heat conduction equations with the source term $Qf(r)$. The heat absorbed from the UV light by the metallic particles is transferred to the solution and thus, gives rise to the buoyancy force, $g\rho_0\beta\Delta T$, which is proportional to gravity g, solvent density ρ_0, thermal expansion coefficients $\beta=\delta\rho/\delta T$ and the temperature difference, ΔT, with respect to a reference value.

Simulations presented in Figure **A-1** show how the fluid in the region irradiated by the UV light (orange circle) heats up and produces convective vortexes, which aggregate polystyrene tracers into clusters that are centered on the spot heated by light and located at the bottom wall. When the source of light is shifted, the tracers follow and assemble at the new position.

The magnitude of the simulated flow velocities (Figure **A-2**) is comparable to the experimental observation presented in Figure **2-3A** and increases in a manner roughly proportional to the concentration of the metallic particles. The simulated structures of the aggregated clusters of tracers, shown in Figure **A-3**, are qualitatively similar to the close-packed arrangement displayed in Figure **2-5**.

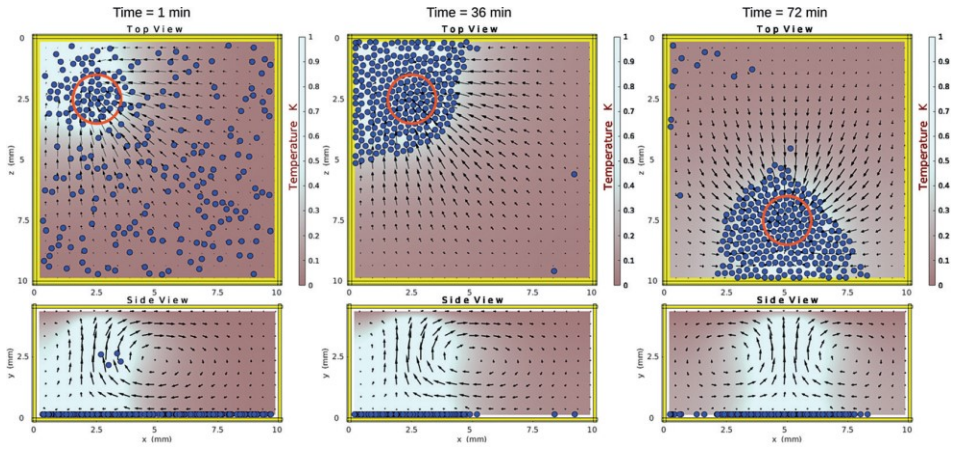

Figure **A-1**: Aggregation of the tracer particles (blue spheres) induced by the heating of the aqueous solution of gold nanoparticles (C=0.005% w/w) by the UV light (red circle). The temperature ΔT (K) distribution is shown with a color-bar. The direction of the fluid velocities is indicated with black arrows. The left and middle panels show sequential stages of the aggregation by the UV light fixed at the position x=z=2.5 mm. The right panel shows the aggregated state induced by the UV light shifted to x=5 and z=7.5 mm.

Detailed Model

Our simulations demonstrate that the mechanism of thermal buoyancy can qualitatively explain the experimental observations reported herein. Thermal buoyancy is generated by heating the metallic particles by UV light. The following stages of energy transduction occur in the system: 1) the energy originating from a radiation source is converted into heat via light absorption by the metallic nanoparticles, 2) the conversion of heat into the thermal expansion of the fluid that produces buoyancy forces driving the fluid motion, and 3) the assembling of the tracer particles by the flow.

We assume that the light source generates a beam of radius R_l=1 mm that has a uniform cross-sectional intensity I (measured in Wm^{-2}). In the model, the metallic particles play the role of the heat sources that drive flows via buoyancy forces. For a fluidic chamber of height H=4.5 mm, all gold particles with diameter D ~ 21 nm and density ρ=19300 $kg \cdot m^{-3}$ sediment to the bottom wall within about 10 days due to the small sedimentation velocity of approximately 4.4 $nm \cdot s^{-1}$. Experimentally observed convective flows (Figure **2-3**) with velocities on the order of 100 $\mu m \cdot s^{-1}$ effectively mix the suspended particles and, therefore, increase the sedimentation time even further. Therefore, we ignore sedimentation effects of the metallic particles and assume that the particles remain uniformly dispersed throughout the chamber within the simulation times (corresponding to less than two hours).

The coordinates $r_i(t)=(x_i(t),y_i(t),z_i(t))$ of the particles that are exposed to the UV light lie within the cross-section of the light beam $x^2 + z^2 \leq R_l$. In the process of light adsorption, each metallic particle generates a heat q (W), which is transmitted to the surrounding fluid. Uniformly distributed metallic particles with concentration C (measured in the number of particles per unit of volume) generate a heat $Q=qC$ (Wm^{-3}), which is transmitted to the unit volume of the solution per unit of time.[2] Thus, to approximate the heat generated in the chamber by the irradiated metallic particles dispersed in the solution, we introduce the function $Q \cdot f(\mathbf{r})$, where the parameter Q (Wm^{-}

^{3}) represents the magnitude of the heat source and the function describes the spatial distribution of the heat sources within the simulation domain:

$$f(x,y,z)=\begin{cases}1, & \text{if } x^2+z^2\le R_l^2 \text{ and } \quad y<H,\\ 0, & \text{otherwise.}\end{cases} \tag{A1}$$

The heated region in the chamber is confined by the radius of the light beam.

The nonuniform temperature distribution within the fluid causes density variations $\Delta\rho=\rho\beta(T-T_0)$, where temperature T is measured with respect to the reference point T_0 (room temperature), $\beta=\dfrac{\partial\rho}{\partial T}$ is the coefficient of the fluid thermal expansion, and ρ_0 is the fluid density at $T=T_0$. The resulting buoyancy force $\Delta\rho\mathbf{g}$ generates fluid motion.

To describe the fluid dynamics, we perform simulations in a rectangular domaine $\Omega=\{(x,y,z):0\le x,z\le L,0\le y\le H\}$, which has horizontal dimensions L and height H. The fluid motion is described by the velocity $\mathbf{u}=(u_x,u_y,u_z)$ and pressure p, the temperature deviation from the room temperature $T-T_0$. The respective governing equations are the continuity, Navier-Stokes (in the Boussinesq approximation[3]) and the heat transfer equations:

$$\nabla\cdot\mathbf{u}=0 \tag{A2}$$

$$\frac{\partial\mathbf{u}}{\partial t}+(\mathbf{u}\cdot\nabla)\mathbf{u}=-\frac{1}{\rho_0}\nabla p+\nu\nabla^2\mathbf{u}-\mathbf{g}\frac{\Delta\rho}{\rho_0} \tag{A3}$$

$$\frac{\partial T}{\partial t}+(\mathbf{u}\cdot\nabla)T=\chi\nabla^2T+\frac{Q}{C_f\rho_0}f(\mathbf{r}) \tag{A4}$$

where ∇ is the spatial gradient operator, v is the kinematic viscosity, χ is the thermal diffusivity, and C_f is the specific heat capacity of the fluid. The latter parameters account for the properties of the host fluid and the uniformly dispersed metallic particles. We require the no-slip boundary conditions for fluid velocities at all solid surfaces, and no heat flux across the side and bottom walls:

$$x = 0, L: \quad \mathbf{u} = \mathbf{0}, \ \frac{\partial T}{\partial x} = 0, \quad y = 0: \quad \mathbf{u} = \mathbf{0}, \ \frac{\partial T}{\partial y} = 0, \quad z = 0, L: \quad \mathbf{u} = \mathbf{0}, \ \frac{\partial T}{\partial z} = 0, \tag{A5}$$

We also assume fixed temperatures at the top wall of the container

$$y = H: \quad \mathbf{u} = \mathbf{0}, \ T = T_0. \tag{A6}$$

Polystyrene tracers (much larger than the metallic particles) were used to experimentally probe and characterize the fluid flows and their effects on the immersed cargo. Recall that the relatively small metal particles are simply modeled as the heat sources. On the other hand, we model the motion of the tracer particles, with fluid velocity $\mathbf{u}$ and specified positions $\mathbf{r}_i(t) = \left(x_i(t), y_i(t), z_i(t)\right)$, by the equation:

$$\frac{\partial \mathbf{r}_i}{\partial t} = \mathbf{u} + \mathbf{e} V_S + \mu \left(\sum_{j=1}^{N} \mathbf{F}^{p-p}(\mathbf{r}_i - \mathbf{r}_j) + \sum_{k=1}^{6} \mathbf{F}^{p-w}(\mathbf{r}_i - \mathbf{r}_i^{w_k}) \right), \quad 1 \le i \le N. \tag{A7}$$

Here $V_S = \frac{2}{9} \frac{(\rho_T - \rho_0)}{\rho_0 \nu} R^2 g$ is the sedimentation velocity of tracers with the density ρ_T, radius R, and mobility $\mu = (6\pi \nu \rho_0 R)^{-1}$. The vector $\mathbf{e} = (0,1,0)$ specifies the direction of the gravity vector $\mathbf{g}$. Vectors $\mathbf{r}_i - \mathbf{r}_i^{w_k}$ specify the distance of particles from the domain walls labeled

by *k*. The inter-particle, $\mathbf{F}^{p-p}(\mathbf{r}) = -\frac{\partial U(r)}{\partial \mathbf{r}}$, and particle-wall, $\mathbf{F}^{p-w}(\mathbf{r}) = -\frac{\partial U(r)}{\partial \mathbf{r}}$, forces were modeled by introducing the Morse potential

$$U(r) = \varepsilon\left(1 - \exp[-\omega(r - r_0)]\right)^2. \tag{A8}$$

The parameters ε and ω denote the strength and width of the potential, respectively, and r_0 is the equilibrium (and cutoff) distance of the potential. We simulate large diameter polystyrene tracers for which the Brownian contribution in eq. (S7) can be ignored.

Simulation Results

To obtain fluid velocities consistent with the experimental observations, we model a rectangular fluidic domain (Figure **A-2**) with horizontal dimensions L= 1cm and height H=0.45cm. We assume that the chamber is filled with water with corresponding parameters ρ_0 ,ν, β, χ, and C_f. We further assume that the concentration of the dispersed metallic particles is relatively low and does not change these parameters. The light source has radius R_l=1mm. The heating parameter Q=qC (proportional to the concentration C of the metallic particles known from the experiment) is tuned to obtain fluid velocities on the order of a hundred of micrometers per second. The energy absorbed by a relatively small (with a radius much smaller than the wavelength of light), single metallic particle can be estimated using Mie theory[4] as

$$q = \frac{8\pi^2 r_{\mathrm{p}}^3}{\lambda} \mathrm{Im}\left[\frac{\varepsilon_{\mathrm{p}} - \varepsilon_{\mathrm{m}}}{\varepsilon_{\mathrm{p}} + 2\varepsilon_{\mathrm{m}}}\right] I. \tag{A9}$$

We assume that all the absorbed energy is converted to heat. We take an example of the experimentally used UV light source with a wavelength λ=320 nm and intensity I=7850 Wm^{-2} , and

gold nanoparticles with the radii r_p=*10.5* nm and complex-valued permittivity ε_p=-0.24+7i [4] (where $i = \sqrt{-1}$ and $\varepsilon_{\mathrm{m}} = 1.77$ is the permittivity of water), and obtain a value q = 1.39 pW, which we use in all simulations.

For computational efficiency, we use a small number of tracer particles N. At the same time, the clusters of particles should be sufficiently large to reveal the arrangement of particles within the clusters. Therefore, we use N = 350 polystyrene particles with radius R = 150 μm. Even though smaller polystyrene tracers (D = 10 μm) are used in the experiment, the correlation between the experimental observations and the simulations indicates that the dynamics of large- and small-sized tracers is controlled by the same physical mechanisms. There are two advantages of simulating relatively larger tracer particles. First, they sediment quickly to the bottom surface (where they assemble into 2D arrays) and, second, they respond more quickly to the imposed convective flows because the flow speed increases essentially linearly away from the bottom wall, where the flow speed is zero (no-slip boundary condition).

The results of typical simulations are shown in the Figure **A-3**. Initially (at time zero), the system is maintained at a reference temperature T_0 and the polystyrene tracers are uniformly dispersed throughout the domain (small blue spheres in Figure **A-3**). The light beam (with circumference outlined by the red circle) heats the fluid that contains uniformly dispersed metallic particles (not shown) and polystyrene tracers. The heat absorbed by the metallic particles locally increases the temperature of the solution and generates convective motion (the direction of the fluid velocities is shown with black arrows). The thermally expanded fluid rises to the top wall of the chamber, forming an upstream flow along the direction of the light. By continuity, the fluid then moves downward along the side walls and inward along the bottom wall. The inward flow drags sedimented tracers along the bottom and assembles them into a 2D array (time = 3 min in Figure

2-3). The final particle arrangement (time = 45 min in Supporting Figure **2-3**) resembles the close packed structures observed in the experiment (Figure **2-5**).

The characteristics of the generated convective flows are demonstrated in Figure **A-2**. The horizontal fluid velocities (monitored at the position x=4 and z=5 mm) depend approximately linearly on the concentration (expressed in weight/weight percent, % w/w) of the metallic particles (as well as on the magnitude of the heat generation described by $Q=qC$ Wm^{-3} Wm-3). Therefore, the dependence shown in Figure **A-2a** is qualitatively similar to that shown in Figure **2-3**A (TiO2 particles in Chapter 2) and Figure **2-9** for the gold particles. The quantitative discrepancy between the experimental results (Figure **2-9**) and simulations (Figure **A-2**) for gold nanoparticles is most likely caused by the asymmetric distribution of the sizes of the gold particles used in the experiments (resulting in different heating q), differences in the geometry of the fluidic chamber (cylindrical in the experiment and rectangular in the simulations), and differences in the theoretical and experimental realizations of the thermal boundary conditions. The fluid profiles (x=4, 0<y<4.5, z=5 mm) corresponding to the increasing fluid velocities are shown in the Figure **A-2**b. The shape of the flow profiles, with the fluid moving to the right near the bottom and to the left near the top (and zero at the boundaries), are qualitatively similar to the experimentally measured profile shown in Figure **2-2**.

Simulations of the migration of the polystyrene tracers toward the source of heat are presented in Figure **A-4**. (Recall that these particles were uniformly distributed over the bottom wall.) First (at time = 1 min), the particles start to aggregate toward the heat source located at x=2.5 and z=2.5 mm. After the aggregation is completed (time = 36 min), the heat source is relocated to the new position at x=5 and z=7.5 mm and the tracers migrate toward the light spot (time = 40 min). After this aggregation is completed (time = 72 min), the heat source is shifted again to the position at x=7.5 and z=2.5 mm where the tracers assemble into a cluster with the close-packed arrangement (time = 108 min). The results qualitatively reproduce the experimentally observed

migration of the tracers reported in Figure **A-1**. Note that the temperature increase in the simulations was on the order of 1K, which is consistent with the experimentally measured heating presented in Figure **2-8**.

Note that the proposed mechanism of aggregation of tracers by convective flows has limitations. In particular, there is a lower bound on the size of tracers because fluid velocities, that determine the drag force on the tracers, decrease as one approaches the wall where the no-slip boundary condition (zero velocity) is realized. Therefore, for sufficiently small tracers, the drag force should decrease as the radius of tracer decreases, slowing down the aggregation. Large heavy tracers will also move slowly.

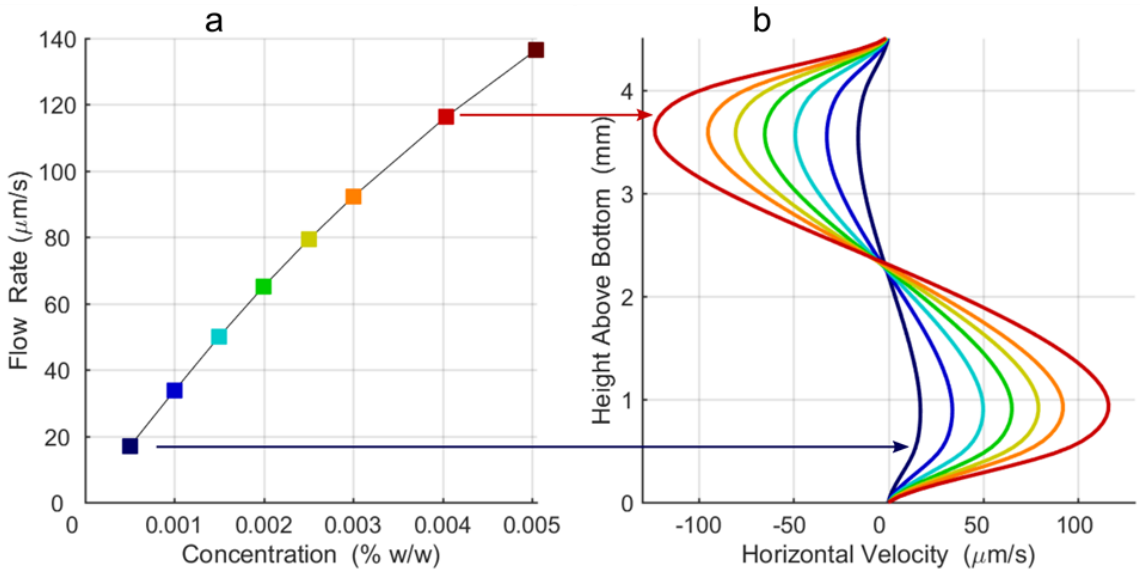

Figure **A-2**: Simulation results for the velocities of thermally generated convective flows. (a) Horizontal fluid velocities increasing with the increasing concentration C (%w/w) of the gold nanoparticles (each generating heat q = 1.4 pW). (b) Horizontal fluid velocities (calculated at x=4 and z=5 mm) as functions of the height above the bottom wall.

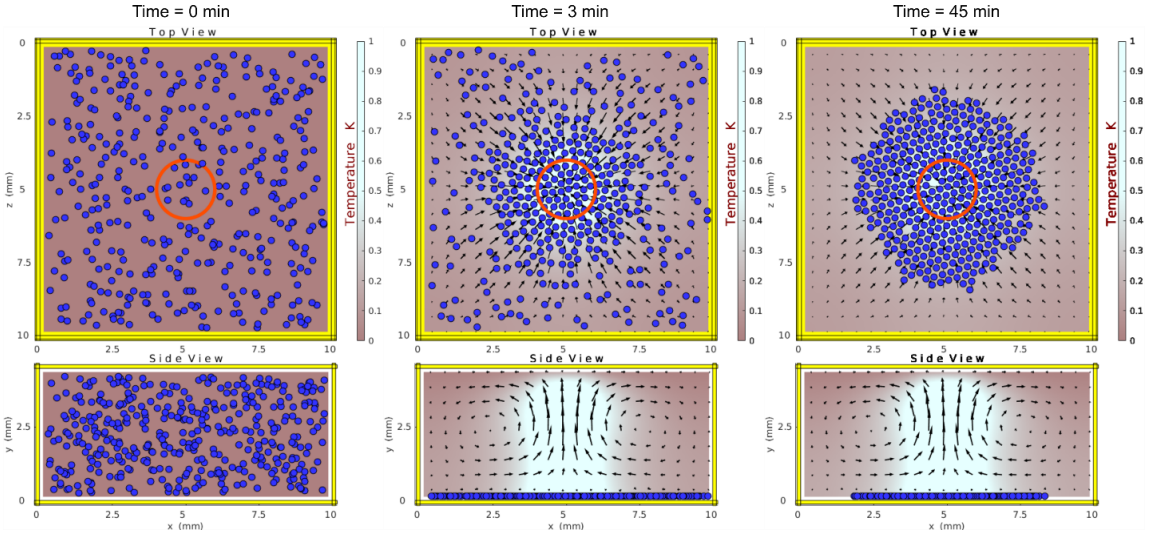

Figure **A-3**: Simulation results for the induced by the UV light convective flow aggregation of the polystyrene tracers (blue spheres) into a cluster with a close-packed arrangement (C=0.005 % w/w, q = 1.39 pW). Initially, tracers are uniformly dispersed throughout the solution and temperature is T_0. The values of temperature T-T_0 (K) are shown by the color-bar. The part of the fluid domain exposed to light is indicated by the red circles in the "Top view" and by the higher temperatures in the "Side view". The directions of the thermally generated flows are shown with black arrows. The Supporting Video 2-7 shows the detailed dynamics of this process.

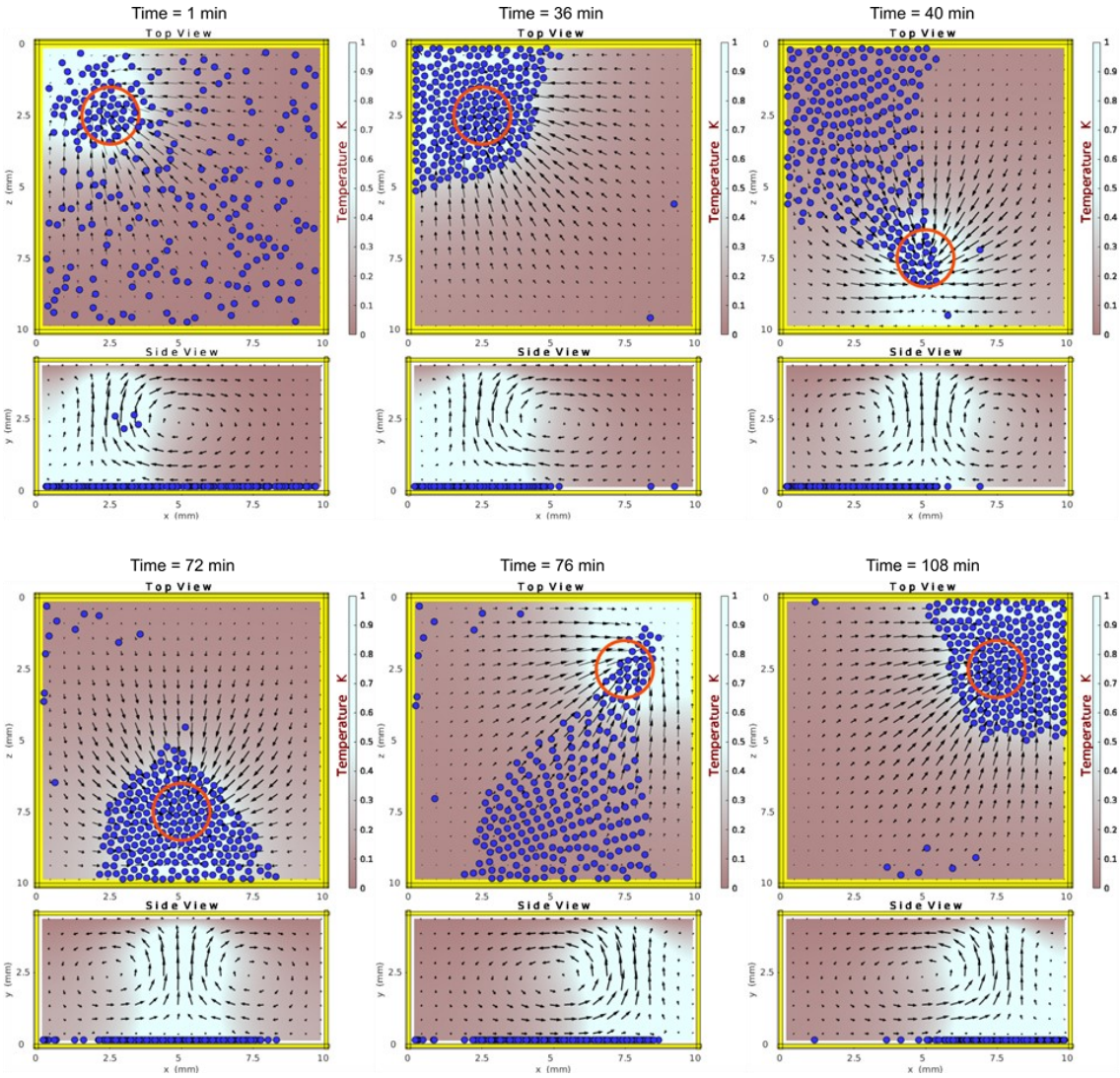

Figure **A-4**: Simulation results for the migration of the tracer particles (blue spheres) due to the relocation of the UV light (red circle). The concentration of gold nanoparticles (not shown) is C=0.005 % w/w and each particle produces heat q = 1.39 pW. The values of temperature T-T_0 (K) are shown by the color-bar. The part of the fluid domain exposed to light is indicated by the red circles in the "Top view" and by the higher temperatures in the "Side view". The directions of the thermally induced flow are shown with black arrows. The Supporting Video 2-8 shows the dynamics of this process.

Thank you to Drs Oleg Shklyaev and Anna Balazs for the work presented in this section.

References

[1] H. H. Richardson, M. T. Carlson, P. J. Tandler, P. Hernandez, A. O. Govorov, *Nano Lett.* **2009**, *9*, 1139-1146.

[2] S. Chandrasekhar, Hydrodynamic and hydro magnetic stability, Oxford, Clarendon, **1961**.

[3] C. F. Bohren and D. R. Huffman, Absorption and scattering of light by small particles, Wiley-VCH, New York, 1983.

[4] E.D. Palik, Handbook of Optical Constants of Solids, New York, Academic Press, **1985**

Appendix B

Downward Pumping of Formate

Although alcohols were the focus of Chapter 4, interesting behavior was observed a few other functional groups. Of particular interest if formic acid. While formic acid pumped upwards (Table **4-1**), sodium formate actually pumped downwards. It was the only analyte for which direction was pH dependent. In this appendix, these results will be briefly discussed.

Results of Formate Trials

When a solution of formic acid (0.217 M) and H_2O_2 (0.49 M) was irradiated with UV light, upwards pumping was observed. As an oxidation product of methanol, it was included in the testing suite alongside formaldehyde, which also pumped upwards. Given these results, it was surprising that sodium formate pumped downwards. A suite of pH values was tested and the change could be seen clearly around a pH value of about 5.2.

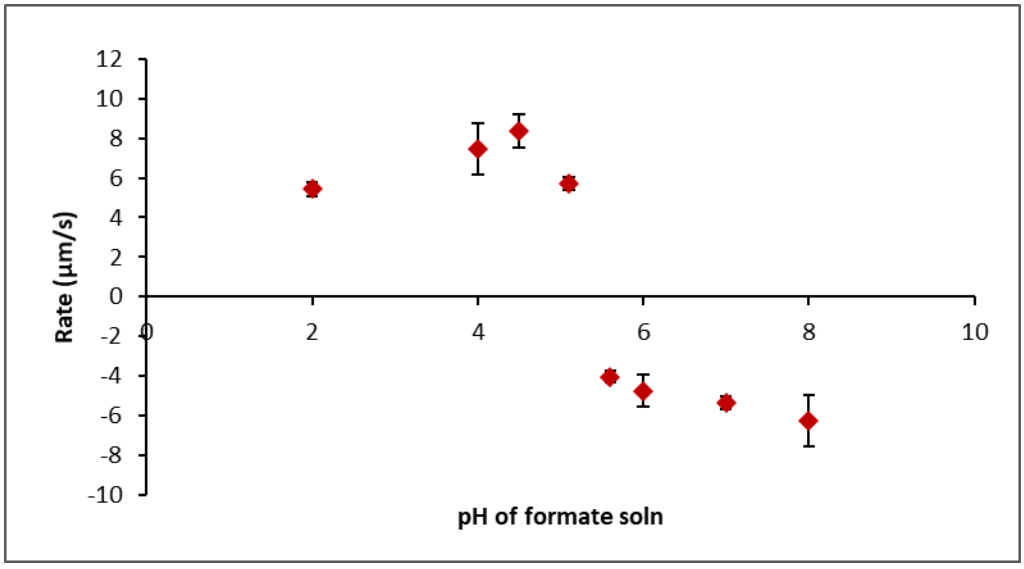

Figure **B-1**: The fluid pumping rate and direction for sodium formate and H_2O_2 at varying pH values. After around pH 5.2, the direction changes. Negative values indicate downward flows.

The probe the reaction in this system, the pH was monitored over time. Under UV irradiation, the pH would increase as the reaction progressed. This is a stark contrast to the decrease observed for ethanol (Figure **4-5**). This indicates that the major product is basic. NMR analysis did not provide any indication of a reaction despite the pH change. From this data, we hypothesize that sodium formate reacts to yield sodium hydroxide, which would go undetected by NMR. The decomposition of sodium formate is known to yield sodium hydroxide and carbon dioxide.[1] Tt is likely that the downward pumping stems from solutal buoyancy flows. Here, the diffusivity of hydroxide ions (the product) is higher than that of formate (the reactants). Since this ratio is greater than one, the weighted ratio of solutal expansion coefficients must be lower than that of the diffusivities in order for the rule to hold. By comparison, formic acid is known to generate carbon monoxide and hydrogen gas as its major decomposition products.[2]

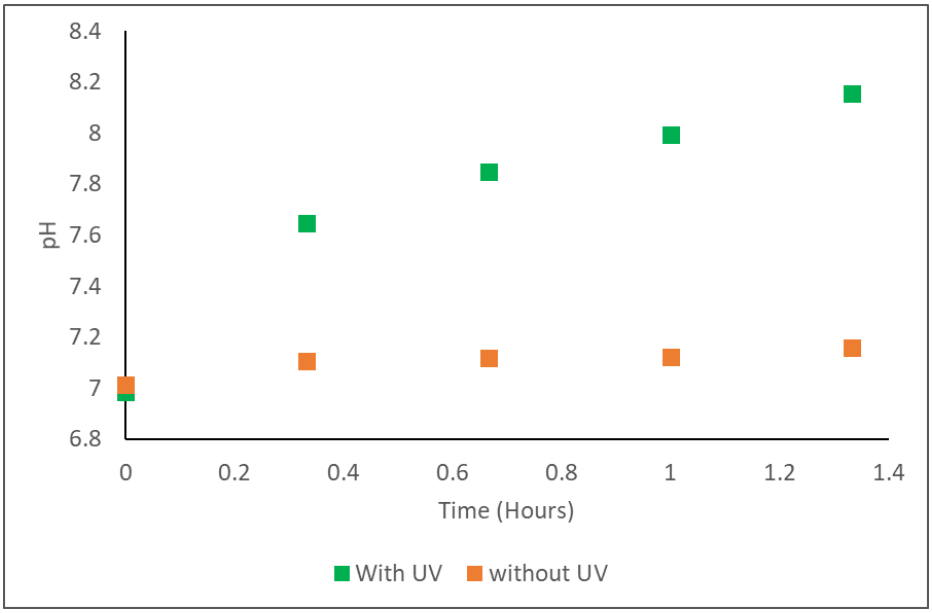

Figure **B-2**: The pH values for sodium formate and H_2O_2 over time. With UV irradiation, the value was seen to steadily increase. Without UV irradiation, little to no change was observed. Measurements were performed in triplicate and all standard deviations were less than 0.1.

Several different salts were chosen in order to test for the presence of ionic gradient effects for the convective pumping phenomenon. These were sodium nitrate, sodium chloride, and sodium

sulfate. None of these prevented the motion despite the high concentrations used. These results support the solutal buoyancy hypothesis. There was a slight decrease in pumping velocity, but this could be attributed to changes in viscosity owing to the high concentrations of salt added.

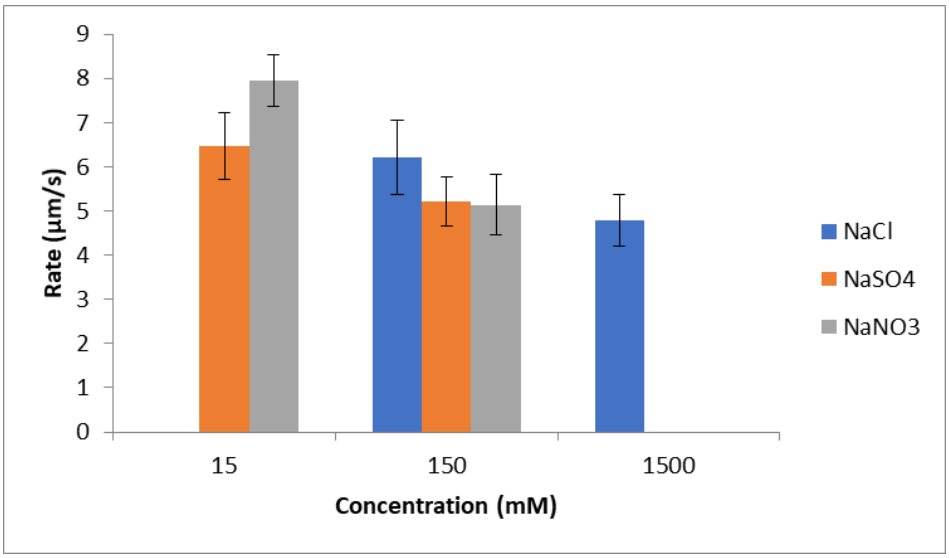

Figure **B-3**: The effect of different salts on the downward flow rate in the system with sodium formate (0.217 M) and H_2O_2 (0.49 M). As shown, no amount of salt would prevent the downward pumping phenomenon. The rates decrease as more salt is added, but this is again attributed to an increase in viscosity with solute.

Experimental

The pH values were adjusted using a Thermo Scientific Orion Star pH meter. The volume used for pH measurements was 900 µL, which required the use of a micro pH probe attachment (Orion™ PerpHecT™ Ross™ Combination pH microelectrode). Either hydrochloric acid or sodium hydroxide was used to adjust the pH for each trial. To monitor pH over time, the same set=up was used. The sample was irradiated for the duration and only removed for long enough to

record the pH values in triplicate (roughly 3-5 minutes). For useful reference, the pKa of formic acid is 3.75, which is lower than the pH at which pumping becomes downwards.

References

[1] A. Farkas, L. Farkas, J. Yudkin, *Proc. R. Soc. Lond. B.* **1934**, *2*, 373–379.

[2] W. L Nelson, C. J. Engelder, *J. Phys. Chem.* **1924**, *30*, 470-475.

VITA

Benjamin Mattson Tansi

Ben grew up in the town of Wrentham, Massachusetts. He then attended Juniata College in central Pennsylvania where he earned a bachelor's degree in chemistry with honors and distinction. Within his first two months, he began conducting research, which continued for all four years. Having developed a passion for discovery, he moved less than an hour away to begin his graduate coursework at the Pennsylvania State University. In 2014, he joined the lab of Ayusman Sen in order to study active systems. After a foray into enzyme micromotors, he became deeply interested in light-based micropumps. Among other achievements, this pursuit has since earned him an invited speaker opportunity at a Gordon Research Conference and a featured cover article in Angewandte Chemie. In his free time, Ben likes to play jazz piano in small ensembles and defensemen for the Vikings in the Nittany Hockey League (NHL).